High-valent [MnFe] and [FeFe] cofactors in ribonucleotide reductases ☆

Nils Leidel [a], Ana Popović-Bijelić [b,1], Kajsa G.V. Havelius [a], Petko Chernev [a], Nina Voevodskaya [b], Astrid Gräslund [b,*], Michael Haumann [a,**]

[a] *Institut für Experimentalphysik, Freie Universität Berlin, 14195 Berlin, Germany*
[b] *Department of Biochemistry and Biophysics, Stockholm University, 10691 Stockholm, Sweden*

ARTICLE INFO

ABSTRACT

Ribonucleotide reductases (RNRs) are essential for DNA synthesis in most organisms. In class-Ic RNR from *Chlamydia trachomatis* (*Ct*), a MnFe cofactor in subunit R2 forms the site required for enzyme activity, instead of an FeFe cofactor plus a redox-active tyrosine in class-Ia RNRs, for example in mouse (*Mus musculus*, *Mm*). For R2 proteins from *Ct* and *Mm*, either grown in the presence of, or reconstituted with Mn and Fe ions, structural and electronic properties of higher valence MnFe and FeFe sites were determined by X-ray absorption spectroscopy and complementary techniques, in combination with bond-valence-sum and density functional theory calculations. At least ten different cofactor species could be tentatively distinguished. In *Ct* R2, two different $Mn(IV)Fe(III)$ site configurations were assigned either $L_4Mn^{IV}(\mu O)_2Fe^{III}L_4$ (metal–metal distance of ~2.75 Å, L = ligand) prevailing in metal-grown R2, or $L_4Mn^{IV}(\mu O)(\mu OH)Fe^{III}L_4$ (~2.90 Å) dominating in metal-reconstituted R2. Specific spectroscopic features were attributed to an $Fe(IV)Fe(III)$ site (~2.55 Å) with a $L_4Fe^{IV}(\mu O)_2Fe^{III}L_3$ core structure. Several $Mn,Fe(III)Fe(III)$ (~2.9–3.1 Å) and $Mn,Fe(III)Fe(II)$ species (~3.3–3.4 Å) likely showed 5-coordinated Mn(III) or Fe(III). Rapid X-ray photoreduction of iron and shorter metal–metal distances in the high-valent states suggested radiation-induced modifications in most crystal structures of R2. The actual configuration of the MnFe and FeFe cofactors seems to depend on assembly sequences, bound metal type, valence state, and previous catalytic activity involving subunit R1. In *Ct* R2, the protonation of a bridging oxide in the $Mn^{IV}(\mu O)(\mu OH)Fe^{III}$ core may be important for preventing premature site reduction and initiation of the radical chemistry in R1.

1. Introduction

Ribonucleotide reductases (RNRs) are the only enzymes that catalyze the reduction of ribonucleotides to their deoxy-forms essential for DNA synthesis in all organisms [1–6]. Class I RNRs found in eukaryotes and certain microorganisms are hetero-tetrameric enzymes of $R1_2R2_2$ organization [7]. The R1 protein contains the nucleotide binding site and R2 contains a dinuclear metal center, which is the catalytic center of dioxygen (O_2) reduction. In the standard case, the metal site in a high-valent state oxidizes a neighboring tyrosine residue to a stable tyrosyl radical, which is an essential step for activation of the enzyme [8]. In class Ia RNRs, e.g. from *Escherichia coli* (*E. coli*) and eukaryotes such as mouse and humans, the metal center contains two iron atoms and thus is of the FeFe type [9].

Only recently, a novel type of RNRs (class Ic) has been discovered in the human pathogen *Chlamydia trachomatis* (*Ct*). In this enzyme, the R2 subunit contains a redox-inert phenylalanine, which is at the position of the usual radical-carrying tyrosine. In addition, R2 harbors a hetero-bimetallic site in its most active form, which consists of a manganese and an iron ion forming a MnFe site [10–12]. The MnFe enzyme is the only RNR encoded in the genome of this organism [13,14]. Closely related MnFe sites have been found in purple acid phosphatases [15], in an N-oxygenase [16], and in a potential monooxygenase [17], suggesting that the *Ct* RNR and these enzymes may belong to a larger family of O_2-activated MnFe enzymes [13,18].

Extensive investigations on FeFe RNRs have established that the catalytic reaction involves activation of an O_2 molecule at the dimetal cluster to generate a high-potential site, which oxidizes the nearby tyrosine residue to a tyrosyl radical, Y• [19–21]. Y• in turn, via a redox cascade of intervening tyrosine and tryptophan residues,

generates a cysteine radical at the substrate binding site in R1, which initiates ribonucleotide reduction [22–26]. Usually, the Y• radical can be observed by EPR in aerobically purified FeFe RNR proteins [27]. In R2 from mouse, this Tyr177 is at ~6 Å distance to the nearest iron atom of the active site [27,28]. In the MnFe RNR of *Ct*, however, in which Phe127 replaces the radical-forming tyrosine, no stable Y• or other amino acid radical was observed. This is true even for the Phe→Tyr mutant [29]. Thus, in the MnFe RNR, the function of the Y• radical in R2, which is to represent the oxidized entity responsible for the reversible initiation of the redox cascade and enzymatic activity in R1, is taken over by the metal site itself. For this function, stabilized high-valent redox states of the metal ions are required [2,13,14,30–32].

For both FeFe and MnFe RNRs, high-valent states of the metal center have been shown to be essential in the electron transfer reactions. At least the $Fe(III)_2$, Fe(IV)Fe(III), and $Fe(IV)_2$ states seem to be involved in the FeFe RNRs [33–35]. The Fe(IV)Fe(III) state, which has been termed "intermediate *X*" [35,36], oxidizes the neighboring tyrosine to Y•. For the MnFe RNR, the Mn(III)Fe(III), Mn(IV)Fe(III), and Mn(IV)Fe(IV) states have been shown to exist and the Mn(IV)Fe(III) state seems to be the functional mimic of the $Y•Fe(III)_2$ moiety in initiating the redox cascade in the R1 subunit [2,13,14,30–32].

High-resolution structural information is indispensable to unravel the individual steps of O_2-activation of the RNR metal sites. Furthermore, it is required to understand the differences in structure and function of the FeFe and MnFe centers. The structural data base contains more than forty crystal structures of R2 proteins of RNRs from various organisms. They mostly contain an FeFe site, but also structures with MnMn, CoCo, or ZnZn sites are available. *Ct* apo-R2 can also be reconstituted with Fe(II) ions so that a typical, but low activity FeFe cofactor is formed [13,14,37]. Two crystal structures with this cofactor have been reported [12,29] and very recently also a structure with a MnFe cofactor [29]. In all structures, the metal ions are coordinated by conserved amino acids, i.e. three glutamate residues and one aspartate (four Glu are found in the *Ct* R2), and two histidines. In addition, a variable number of terminal metal-bound oxygen species (H_2O or OH), metal-bridging oxo (μO) or hydroxo (μOH) groups, and carboxylates in various coordination configurations were detected [32].

X-ray irradiation induced reduction of high-valent metal ions in proteins is a problem in the determination of three-dimensional structures by crystallography, in particular when metal sites with high redox potential, as the ones in RNR, are studied [38–40]. Analysis of the crystal structures by bond-valence-sum (BVS) calculations [41] reveals that in none of them the apparent mean metal oxidation state exceeds ~2.5; the average value is close to 2 (Figs. 1 and S1). This means that it is likely that in the proteins with initial $(III)_2$ metal oxidation state, one or both metal ions had become reduced during diffraction data collection. Accordingly, the functional relevance for the various metal coordination geometries in the protein crystals and their relation to the metal oxidation state is unclear. Also the effects of site-directed mutations are ambiguous. Crystal structures of R2 containing high-valent metal sites presumably are not available so far.

X-ray absorption spectroscopy (XAS) is a method by which atomic-resolution structural information also on high-valent metal sites can be obtained [42–44]. However, only few XAS studies on RNRs have been reported [9,32,45–49]. The MnFe site in *Ct* RNR has been investigated by XAS previously by us and other authors [32,45]. An apparent discrepancy exists with respect to the structure of the Mn(IV)Fe(III) state, for which a metal–metal distance of ~2.75 Å was proposed in Ref. [32], but of ~2.9 Å in Ref. [45]. One difference in the two studies was that in Ref. [32] recombinant R2 protein was grown in the presence of Mn and Fe ions, whereas in Ref. [45] metal-reconstituted recombinant R2 protein was used. The exact sample conditions may therefore possibly influence the structure of the metal site.
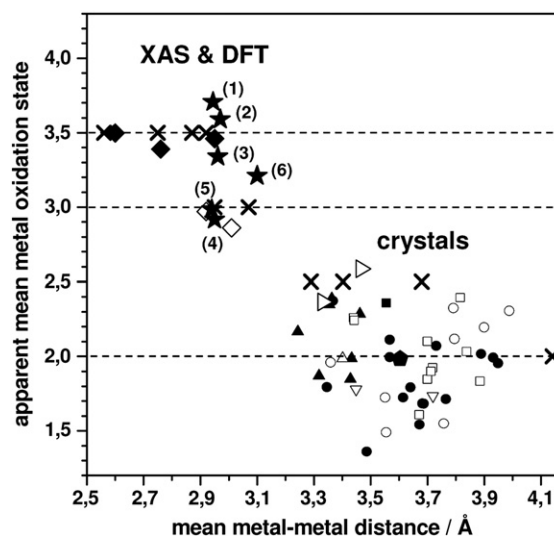
Fig. 1. Metal oxidation states and distances in R2 subunits of RNRs. BVS values (see Materials and methods) on the y-axis are used as a measure of the apparent metal oxidation state. For further correlations see Fig. S1. BVS of metal sites in R2 crystals in the data base (given oxidation states follow assignments in the respective data files): ● $Fe(III)_2$; ○ $Fe(II)_2$; ▲ Fe_2 (valences not specified); ■ $Mn(III)_2$; □ $Mn(II)_2$; △ $Co(III)_2$; ▽ $Zn(II)_2$; ▷ $Fe(II)_2$ in *Ct* R2 (1ANI, 1SYY); ⬟ average BVS from all crystal data above. Mean BVS of first-sphere metal–ligands and mean metal–metal distances from Fe and Mn EXAFS data in this work (Table 4, Fig. 7), ★: (1) *Ct*R2$^g_{MnFe}$, (2) *Ct*R2$^r_{MnFe}$, (3) *Ct*R1R2$^g_{MnFe}$, (4) *Ct*R1R2$^r_{FeFe}$, (5) *Ct*R2$^g_{FeFe}$, (6) *Mm*R2$^r_{FeFe}$. BVS and metal–metal distances of DFT structures (Fig. 10): ◆ Fe,Mn(IV)Fe(III) states and ◇ Fe,Mn(III)Fe(III) states. BVS values for DFT structures were multiplied by 1.06 to include a possible mean overestimation of bond lengths by 0.02 Å. ✕ data for pure oxidation states and respective metal–metal distances from EXAFS as assigned in the present and previous [32] investigations.

In the present work, XAS at the Mn and Fe K-edges was employed to compare FeFe and MnFe cofactors in RNR from *Ct* and mouse (*Mus musculus*, *Mm*) in their higher valence states. Metal reduction by X-rays is rapid and thus difficult to avoid in crystallography, but allowed us to estimate relative redox potentials for the metal sites. Structural properties from XAS, in particular metal–metal distances, and electronic features from X-ray emission spectroscopy and EPR, are reported, e.g., for Fe(IV)Fe(III) and Mn(IV)Fe(III) sites. Two Mn(IV)Fe(III) configurations are proposed based on the XAS data, which resolves the apparent controversy in the literature. Structural and electronic features are interpreted with regard to model structures as derived from density functional theory (DFT) calculations.

2. Materials and methods

2.1. Protein sample preparation

Recombinant *Ct* R2 RNR protein was overexpressed in *E. coli* strain BL21(DE3) containing pET3a-R2 plasmids encoding wild-type R2 protein. Recombinant mouse (*Mm*) R2 RNR protein was overexpressed in Rosetta 2(DE3)pLysS strain containing pET-R2 plasmids encoding native mouse R2 protein. Bacteria were grown in LB medium (with and without metal supplements) at 37 °C to a 595 nm absorption of 0.8, induced with 500 μM isopropyl-1-thio-β-D-galactopyranoside (IPTG), further grown for 20 h at 17 °C, and harvested. For cells grown in Mn-enriched LB medium, 80 μM $MnCl_2$ was added after induction with IPTG [32]. *Ct* and *Mm* RNR proteins were purified as described before [11,50]. Protein (polypeptide) concentrations were derived photometrically using extinction coefficients at 280 nm of 138660 M^{-1} cm^{-1} and 57750 M^{-1} cm^{-1} for *Ct* R1 and R2, respectively [13], and 62,000 M^{-1} cm^{-1} for *Mm* R2 [50].

The following protein samples were prepared. (1) *Ct* R2 RNR protein as purified from *E. coli* cells grown in Mn-enriched LB medium

(Fe and Mn concentrations of 8 and 30 μM), further on is denoted **CtR2$^g_{MnFe}$**. (2) *Ct* R2 RNR apoprotein reconstituted with Mn and Fe (R2 protein was purified from *E. coli* cells grown in the standard LB medium, metals were removed, and the apoprotein was metal-reconstituted as described previously [13,51]) is denoted **CtR2$^r_{MnFe}$**. (3) Sample CtR2$^g_{MnFe}$ was incubated with a catalytic mixture and hydroxyurea [37] according to the following procedure: 200 μM R1 was incubated with 50 mM KCl, 10 mM DTT, 1.2 mM MgCl$_2$, 0.4 mM ATP in 50 mM Tris–HCl buffer, pH 7.6 for 1 min; 200 μM R2 and 2 mM CDP were added; the mixture was incubated for 5 min at room temperature and 1 mM hydroxyurea was added; the sample was frozen in liquid nitrogen after 20 min incubation at room temperature. This sample is denoted **CtR1R2$^g_{MnFe}$**. (4) *Ct* R2 RNR apoprotein reconstituted with Fe and incubated with the catalytic mixture according to the following procedure: R2 protein was purified from *E. coli* cells grown in the standard LB medium, metals were removed, and the apoprotein was reconstituted with an anaerobic solution of Fe(H$_4$N)$_2$(SO$_4$)$_2$ at a ratio of 6 Fe(II) ions per R2 monomer [11,51]; 200 μM R1 protein was incubated with 50 mM KCl, 10 mM DTT, 1.2 mM MgCl$_2$, 0.4 mM ATP in 50 mM Tris–HCl buffer, pH 7.6 for 1 min; 200 μM R2 protein and 2 mM CDP were added; the sample was frozen in liquid nitrogen after 10 min incubation at room temperature. This sample is denoted **CtR1R2$^r_{FeFe}$**. (5) *Ct* R2 RNR protein as purified from *E. coli* cells grown in TB medium (14 μM Fe) is denoted **CtR2$^g_{FeFe}$**. (6) Purified *Mm* R2 RNR apoprotein was reconstituted with an anaerobic solution of Fe(NH$_4$)$_2$(SO$_4$)$_2$ at a ratio of 10 Fe(II) ions per R2 monomer and after incubation for 30 min on ice, excess iron was removed by gel filtration. This sample is denoted **MmR2$^r_{FeFe}$**.

2.2. Metal content quantification

Metal contents of protein samples were quantified by total-reflection X-ray fluorescence analysis (TXRF) [32,52] on a PicoFox spectrometer (Bruker) using a gallium metal standard (Sigma) and the respective protein concentrations, expressed as R2 polypeptide concentrations.

2.3. EPR spectroscopy

9.5 GHz X-band EPR spectroscopy was carried out on a Bruker E580 ELEXSYS spectrometer with samples kept at 20 K in a helium cryostat (Oxford). For spectrometer settings see figure captions. Spin quantification was done by comparison of the double integrated signal of RNR samples with that of a CuSO$_4$-standard. Spectral simulations were carried out with the MatLab (MathWorks) toolbox Easy-Spin [53] as described in Refs. [32,37]. R2 protein concentrations in EPR samples are given in Table 1.

2.4. Optical absorption spectroscopy

Absorption spectra were recorded on a Cary50 spectrometer using aliquots of the protein samples for XAS, which were diluted by a factor of 100 in Tris–HCl buffer (10 mM, pH 7.0).

2.5. Resonance Raman spectroscopy

Raman scattering spectra were measured on a Jobin Yvon XY spectrometer using sample excitation by the 647 nm emission line of a krypton laser (1 mW); samples were held in a liquid nitrogen cryostat (Linkam) at 80 K [54]. Displayed spectra resulted from data acquisition at a resolution of ~0.5 cm^{-1} for 15 min each.

2.6. X-ray spectroscopy

X-ray absorption spectroscopy (XAS) was performed at beamline KMC-1 of BESSY (Helmholtz-Center Berlin) using a double-crystal Si [111] monochromator. Kα-fluorescence-detected XAS spectra at the Fe and Mn K-edges were collected at 20 K using an energy-resolving 13-element Ge detector (Canberra) and a helium cryostat (Oxford) as previously described [32]. Detector-deadtime corrected XAS spectra (scan duration ~30 min) were averaged (8–12 scans) after energy calibration using an Fe foil or a KMnO$_4$ sample as energy standards [55,56]. EXAFS spectra were derived using E_0 values of 7112 eV (Fe) and 6540 eV (Mn); E_0 refined to 7120 ± 2 eV and 6547 ± 1 eV in the least-squares simulations of unfiltered k^3-weighted spectra (in-house program SimX [57], phase functions calculated by FEFF8 [58,59], amplitude reduction factors, S_0^2, of 0.9 (Fe) and 0.85 (Mn)). The given error sum (R_F) is defined as the deviation in % between the Fourier-filtered k-space EXAFS data in the fit range and the fit curve [57].

The distance resolution of EXAFS data may be calculated according to $\Delta R = \pi/2\Delta k$, with Δk being the k-range of data in the simulation. For the k-ranges of Mn (~10.5 Å^{-1}) and Fe (~14.5 Å^{-1}) data, the resolution was estimated as ~0.15 Å (Mn) and ~0.11 Å (Fe), which is smaller or about equal to the distance spread found in the fits of the EXAFS data. The development of satisfactory EXAFS simulation models involved gradual refinement of the fit approach by the inclusion of additional metal-backscatterer shells (see SI). By fixing, e.g., the Debye–Waller parameters ($2\sigma^2$) to physically meaningful values, it was assured that only a reasonably low number of unrestricted fit parameters was used in the simulations.

The pre-edge features in the XANES were extracted using the program XANDA [60] and fitted by Gaussian functions. K-edge energies were determined by the "integral method" (integration limits of 15% and 90% of normalized fluorescence) [57]. For R2 protein concentrations in the X-ray spectroscopy samples see Table 1.

Higher-resolution Fe K-edge measurements, X-ray photoreduction studies, and X-ray emission spectroscopy (XES) at the Fe Kß emission line were done at beamline ID26 of the European Synchrotron Radiation Facility (ESRF) at Grenoble (France). The incident energy was set by a Si[311] double-crystal monochromator (spot size on the sample of ~1×0.2 mm^2, photon flux ~4×10^{12} s^{-1}). Higher harmonics were suppressed by two Si-coated mirrors in total reflection mode. Emission detection using a vertical-plane Rowland-circle spectrometer [61] with 5 spherically-bent Ge wafers at $R = 1000$ mm yielded an energy bandwidth of ~1 eV (Ge[620] Bragg reflection). An avalanche photodiode was used as a detector. Samples were held in a liquid-helium cryostat at 20 K. Kß-fluorescence detected XANES spectra were measured in 5 s using the rapid-scan mode of ID26 [62]. Kß

Table 1
Concentrations of R2 protein monomers, metal contents, and FeFe and MnFe site populations in R2 samples. Metal contents were derived from spectra as in Fig. 2. Amounts of MnFe and FeFe sites represent upper limits, neglecting single-occupancy and potential small amounts of (mixed-metal) Zn- or Cu-containing sites.

Sample	R2 [mM]	Mn [mM]	Fe [mM]	Zn [mM]	Mn/R2	Fe/R2	Zn/R2	Fe/Mn	MnFe [%]	FeFe [%]
*Ct*R2$^g_{MnFe}$	1.7	0.60	0.94	0.18	0.35	0.55	0.11	1.57	78	22
*Ct*R2$^r_{MnFe}$	1.8	0.72	1.70	0.06	0.40	0.94	0.03	2.36	63	37
*Ct*R1R2$^g_{MnFe}$	1.5	0.46	1.28	0.43	0.31	0.85	0.27	2.78	53	47
*Ct*R1R2$^r_{FeFe}$	2.6	0.02	5.92	0.45	0.01	2.27	0.17	296	<1	>99
*Ct*R2$^g_{FeFe}$	3.6	0.04	3.28	0.23	0.01	0.91	0.06	82	2	98
*Mm*R2$^r_{FeFe}$	1.4	<0.01	3.10	0.17	<0.01	2.21	0.12	>500	<1	>99
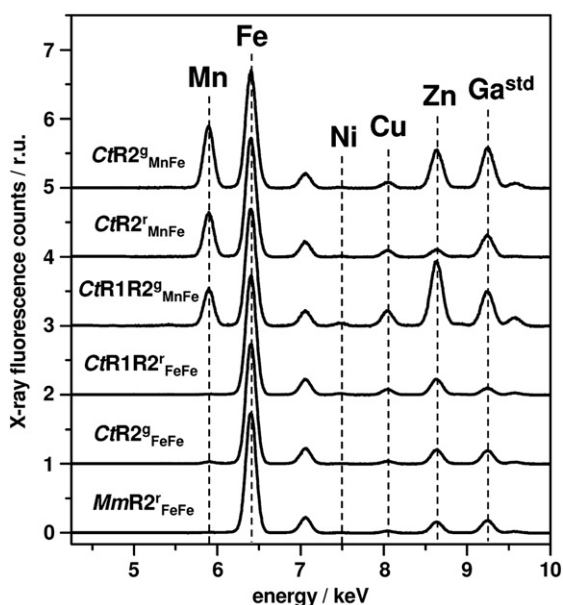
Fig. 2. TXRF spectra of RNR proteins. Spectra were normalized on the Fe Kα X-ray fluorescence line and vertically displaced. A Ga standard (std) was present in all samples. The Kα fluorescence lines of metals are marked, other features show Kβ emission lines.

emission lines were measured within 7035–7070 eV (100 data points, 0.1 s acquisition per data point, off-resonance excitation at 7600 eV). The X-ray beam was attenuated by Al foils until no photoreduction could be detected. X-ray photoreduction at the Fe K-edge was followed using the timescan technique [62]. Kβ emission lines were calculated by a multiplet approach using the program CTM (version 3.11) [63].

2.7. Bond-valence-sum (BVS) calculations

Calculations were done using Eq. (1) [64] and the following parameters: $\beta = 0.37$ Å; values of R_{0i} for Fe–O of 1.737 Å, Fe–N of 1.792 Å, Mn–O of 1.762 Å, Mn–N of 1.843 Å, Co–O of 1.678 Å, and Co–N of 1.735 Å were used. These values represent the average over literature data for metal(II)- and metal(III)–ligand bonds [64–67]; R_0 was 1.718 Å for Zn(II)–O and 1.704 Å for Zn(II)–N [68]. In addition, metal–ligand bond lengths (R_i) from crystal structures (including O and N atoms within a radius of 2.7 Å around each metal ion and calculating the average over all metal ions in a structure data file) or EXAFS were utilized (the sum is over all first-sphere ligand species, i, weighted by their coordination numbers, N_i).

$$BVS = \Sigma N_i \exp[(R_{0i} - R_i)/\beta]. \qquad (1)$$

2.8. Density functional theory calculations (DFT)

Spin-unrestricted geometry optimizations and calculations of electronic parameters of structural models of the metal sites were performed using the ORCA program [69] as described previously [70]. Geometry optimizations involved the BP86 exchange-correlation functional [71] with a triple-zeta valence (TZVP) basis set [72] with one set of polarization functions used for all atoms in the models (SI, Table S2). The resolution-of-identity (RI) approximation was used with the auxiliary TZV/J Coulomb fitting basis set [73]. A dielectric constant of $\varepsilon = 4$ in a COSMO solvation model [74] was used. To derive the correct spin coupling of the two metal atoms, the broken-symmetry formalism using the flip-spin technique as implemented in ORCA [75,76] was applied: first, the high-spin, ferromagnetic state of the system was calculated, then, in order to produce

a starting electron density in which the two metal atoms had opposite spins, the alpha- and beta-spin blocks of the electron density at one of the metal atoms were exchanged; finally, starting from this state, the system was converged to the final anti-ferromagnetic solution. During the geometry optimizations, the C_α atom of each amino acid residue was fixed at its crystallographic position in structure 1SYY (PDB entry number) of wildtype Ct R2. Mulliken population analysis was performed as implemented in ORCA.

3. Results

3.1. Protein samples investigated

The following RNR protein samples were analyzed; the respective R2 polypeptide concentrations are shown in Table 1: (1) CtR2$^g_{MnFe}$, Ct R2 grown with Mn and Fe; (2) CtR2$^r_{MnFe}$, Ct R2 reconstituted with Mn and Fe; (3) CtR1R2$^g_{MnFe}$, Mn,Fe-grown Ct R2 incubated with a catalytic mixture, R1, and the inhibitor hydroxyurea; (4) CtR1R2$^r_{FeFe}$, Fe-only reconstituted Ct R2 incubated with a catalytic mixture and R1; (5) CtR2$^g_{FeFe}$, Ct R2 grown with Fe only; and (6) MmR2$^r_{FeFe}$, Fe-only reconstituted mouse R2. The sample preparation procedures were designed such that distinct structural motifs and oxidation states of the MnFe and FeFe sites in R2 prevailed [11,32,50,51].

3.2. Contents of MnFe and FeFe sites

Quantification of metal contents by TXRF (Fig. 2) and of protein concentrations of RNR samples allowed estimation of MnFe and
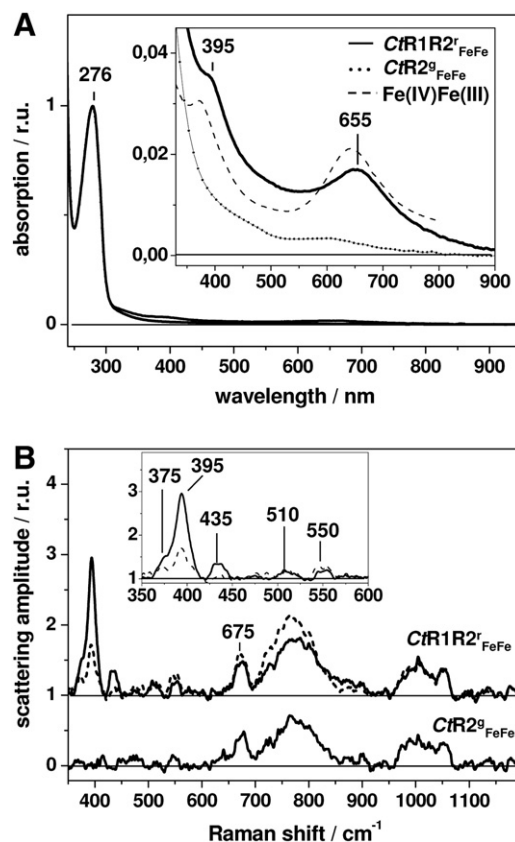
Fig. 3. Optical absorption and Raman scattering of the Fe(IV)Fe(III) state. (A) Absorption spectra of CtR1R2$^r_{FeFe}$ (26 μM R2) and CtR2$^g_{FeFe}$ (36 μM R2) normalized at 276 nm. Inset: magnification of bands at ~655 nm. The scaled spectrum of a synthetic R2 active site mimic, [Fe$_2$(O)$_2$(5-Me-PA)$_2$](ClO$_4$)$_3$],[78] in an Fe(IV)Fe(III) state is shown for comparison. (B) Raman spectra at 80 K of CtR1R2$^r_{FeFe}$ (top) and of the same sample annealed at ~20 °C for 3 h (dashed line), and CtR2$^g_{FeFe}$ (bottom). Inset: close-up of low frequency bands of CtR1R2$^r_{FeFe}$.

FeFe site amounts in the R2 proteins (Table 1). Fe-only reconstituted proteins from both *Ct* and *Mm* showed near-quantitative occupation of R2 by close to two Fe ions per polypeptide chain. As-grown proteins contained substoichiometric metal amounts and thus also empty or singly-occupied sites. Mn was only detected in Mn,Fe-grown or -reconstituted *Ct* samples; the average Fe per Mn ratio of ~2 is similar to previous data [32,77]. Zn levels were elevated in the as-grown samples, increased in the presence of R1 protein, and almost as high as the Mn content in *Ct*R1R2$^g_{MnFe}$. A similar trend at lower concentrations was found for Cu (Fig. 2). Neglecting possible MnMn and Zn/Cu containing sites, metal site contents of 55–80% for MnFe and 20–45% for FeFe in the Mn,Fe-grown or -reconstituted *Ct* R2 samples and ~100% for FeFe in Fe-reconstituted R2 of *Ct* and *Mm* were estimated (Table 1).

3.3. Optical absorption and resonance Raman on CtR1R2$^r_{FeFe}$ protein

Visual inspection revealed a strong green color only for sample *Ct*R1R2$^r_{FeFe}$, which was obtained after incubation of the *Ct* FeFe R2 with the catalytic mixture and R1. The color was stable in samples frozen in liquid nitrogen (77 K) for months, but faded out at room temperature within hours. The electronic absorption spectrum of *Ct*R1R2$^r_{FeFe}$ revealed increased intensity in the range of 350–900 nm with two distinct peaks at ~395 nm and ~656 nm, which were missing in the spectrum of *Ct*R2$^g_{FeFe}$ (Fig. 3A). Rather similar spectra have been reported for synthetic Fe(μO)$_2$Fe model complexes of the R2 active site (see Fig. 3A for an example) and attributed to Fe(IV)Fe(III) states [78,79].

The Raman scattering spectrum of *Ct*R1R2$^r_{FeFe}$ showed prominent vibrational bands in the 350–550 cm^{-1} region. Their magnitudes

Fig. 4. EPR spectra at X-band of RNR protein samples at 20 K. Spectra were recorded for a microwave frequency and power (MP) of ~9.4 MHz and 20 mW and a modulation amplitude (MA) of 10 G, and scaled and vertically displaced for comparison. Open circles show simulations with previously determined EPR parameters [32,77]. Left inset: spectrum of *Ct*R2$^r_{MnFe}$ after subtraction of a small Mn(II) contribution, asterisks mark additional band features. Right inset: spectra (vertically displaced, MA = 3 G) of *Ct*R1R2$^r_{FeFe}$ (top, Fe(IV)Fe(III) signal; MP = 2 mW) and *Mm*R2$^r_{FeFe}$ (bottom, Tyr• radical signal; MP = 50 μW).

Table 2
Quantification of paramagnetic states by EPR. Spins per R2 monomer were derived using double-integration of spectra in the $g=2$ region in Fig. 4, comparison to a CuSO$_4$ spin standard, and protein concentrations in Table 1. The error is about 0.1 spin per R2.

Sample	$g\approx2$ signal	Spin/R2
*Ct*R2$^g_{MnFe}$	Mn(III)Fe(III)	0.2
*Ct*R2$^r_{MnFe}$	Mn(III)Fe(III)	0.2
*Ct*R1R2$^g_{MnFe}$	Mn(III)Fe(III)	0.7
*Ct*R1R2$^r_{FeFe}$	Fe(IV)Fe(III)	0.2
*Ct*R2$^g_{FeFe}$	(EPR-silent)	–
*Mm*R2$^r_{FeFe}$	Tyr$^{\bullet}$-radical	≥0.9

decreased by ~50%, in parallel to the absorption at ~655 nm, in the same sample upon annealing at ~20 °C for 3 h. Similar bands were completely absent in *Ct*R2$^g_{FeFe}$ (Fig. 3B). Unresolved bands in the 650–850 cm^{-1} region were alike in *Ct*R1R2$^r_{FeFe}$ and *Ct*R2$^g_{FeFe}$, but increased in amplitude in the annealed *Ct*R1R2$^r_{FeFe}$, as was a band at 550 cm^{-1}. Similar bands at 950–1050 cm^{-1} in all three samples suggest protein resonances (Fig. 3B). The 395 cm^{-1} band of *Ct*R1R2$^r_{FeFe}$ is at the lower frequency limit of symmetric Fe–μO–Fe vibrational modes in synthetic iron compounds [80–82]. The band at 550 cm^{-1} and features at 650–850 cm^{-1} may show Fe–OH motifs [83]. Bands at 850–900 cm^{-1} due to iron-bound peroxide [84–86] or at 750–850 cm^{-1} due to Fe(IV)=O bonds [87] were not found in *Ct*R1R2$^r_{FeFe}$. We attribute the 395 cm^{-1} vibration and bands at 375 cm^{-1} and 435 cm^{-1} to a special FeFe site configuration only present in *Ct*R1R2$^r_{FeFe}$. The above results and the EPR and XAS data below seem to suggest that this species may be an Fe(IV)Fe(III) cofactor, which converts upon annealing to an Fe(III)Fe(III) species similar to that found in *Ct*R2$^g_{FeFe}$. We note that, e.g., ^{18}O-isotope labeling would be required for unambiguous assignment of the Raman bands, i.e. to an Fe(IV)-containing site.
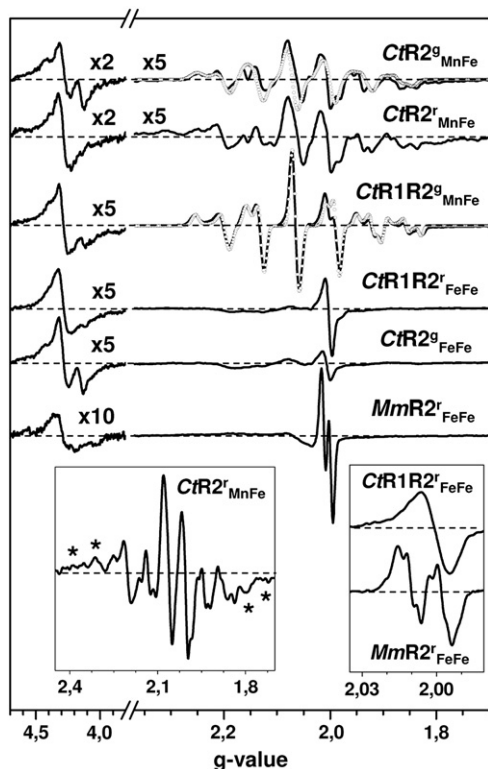
3.4. Paramagnetic states studied by EPR

Mn(III)Fe(III), Mn(II)Fe(II), Fe(III)Fe(II), and Fe(IV)Fe(III) sites are paramagnetic and EPR-detectable, in contrast to mixed-valence MnFe and equal-valence FeFe sites [29,37,88]. In Fig. 4, EPR spectra of the six RNR samples are compared.
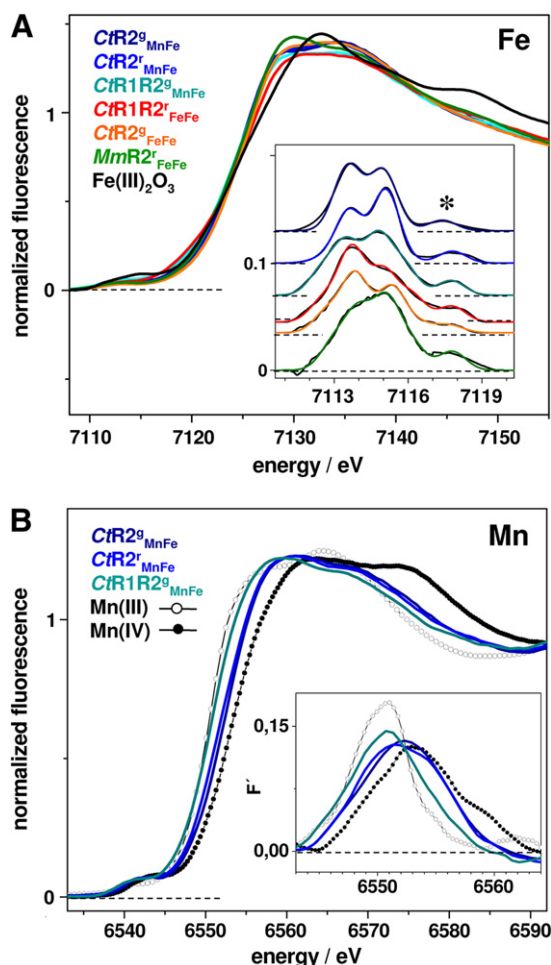
3.4.1. EPR signals around g = 2

The prominent EPR spectrum of *Ct*R1R2$^g_{MnFe}$ is due to a Mn(III)Fe(III) state trapped by the inhibitor hydroxyurea after catalytic turnover of the R1R2 complex [32,37,88]. It reflects antiferromagnetic coupling of high-spin Mn(III) (S = 2) and Fe(III) (S = 5/2) ions in a ground-state S = 1/2 system [32,37,77,88]. Simulation (Fig. 4) was achieved using previously determined g-tensor values [37,77]. Spin quantification assigned this state to ~70% of the protein in *Ct*R1R2$^g_{MnFe}$ (Table 2). Mn(II) signals were not clearly detectable in the EPR spectra and the Mn(II) content thus was below about 5%.

The EPR spectra of *Ct*R2$^g_{MnFe}$ and *Ct*R2$^r_{MnFe}$ differed from the one of *Ct*R1R2$^g_{MnFe}$ (Fig. 4). Their intensities corresponded to ~0.2 spins per R2 in both the former samples (Table 2). These spectra mostly were due to a Mn(III)Fe(III) site in R2 not in contact with R1, which differs from the hydroxyurea-inhibited Mn(III)Fe(III) site in the R1R2 complex [32,77]. The spectrum of *Ct*R2$^g_{MnFe}$ was well simulated with parameters from Ref. [32] (Fig. 4). Additional features in the *Ct*R2$^r_{MnFe}$ spectrum could be due to a small (~15%) contribution from a Mn(IV)Mn(III) site [89,90]. Mn(III)Fe(III) and Mn(IV)Mn(III) states thus were minor species in *Ct*R2$^g_{MnFe}$ and *Ct*R2$^r_{MnFe}$, which mostly contained EPR-invisible Mn(IV)Fe(III) sites.

In the Fe-only samples (*Ct*R1R2$^r_{FeFe}$, *Ct*R2$^g_{FeFe}$, *Mm*R2$^r_{FeFe}$), broad signals around g = 2 were absent, due to the dominance of

Fig. 5. XANES spectra of RNR samples. (A) Fe K-edges of protein samples and of Fe(III)$_2$O$_3$ shown for comparison. Inset: isolated pre-edge features from high-resolution K-edge spectra. Black lines, experimental data; coloured lines, simulations using Gaussian functions (FWHM = 1.3 eV) with parameters in Table 3 and an additional band at ~7117.8 eV (asterisk). Spectra were vertically displaced for comparison. (B) Mn K-edges of protein samples and of Mn(IV) [128] and Mn(III) [129] reference compounds [105]. Inset: first derivatives of spectra.

Fe(III)Fe(III) states. The narrow signal of CtR1R2$^r_{FeFe}$ (Fig. 4, right inset) in ~20% of the protein (Table 2) has been assigned to an Fe(IV)Fe(III) state [29,36,91]. This signal was not obvious in the other Fe-only samples. A minor contribution of the signal (in <10% of protein) may be found in the CtR1R2$_{MnFe}$ spectrum as well. Mouse R2 (MmR2$^r_{FeFe}$) showed near-quantitative amounts of the typical stable tyrosine radical signal, which was absent in the Ct samples (Fig. 4).

Table 3

Mn and Fe K-edge energies and Fe pre-edge peak areas and Kß^{1,3} emission line energies of RNR samples. Pre-edge areas (A) resulted from Gaussian fits of spectra in Fig. 5A with peak energies (± 0.2 eV) of 7113.7 eV and 7115.1 eV and (in parenthesis) 7112.6 eV and 7116.2 eV. Kß^{1,3} energies refer to the calculated first moment [127] within 7154–7164 eV of spectra in Fig. 8. Parameters of reference substances (Mn(IV), Mn$^{IV}_2$ compound [128]; Mn(III), Mn$^{III}_2$ compound [129]; Fe$^{III}_2$O$_3$) (Fig. 5) are given for comparison.

| Sample	E_{edge} [eV] (Mn; Fe)	$A_{pre-edge}$ [r.u.] (Fe)	$E_{Kß1,3}$ [eV] (Fe)
CtR2$^g_{MnFe}$	6551.4; 7123.0	8.3, 7.7 (0.8, 0.2)	n.d.
CtR2$^r_{MnFe}$	6550.9; 7122.9	6.7, 9.4 (0.5, 0.1)	7058.9
CtR1R2$^g_{MnFe}$	6549.9; 7122.6	6.4, 7.3 (3.0, 3.6)	7058.9
CtR1R2$^r_{FeFe}$	-; 7122.4	9.2, 6.2 (2.8, 3.3)	7058.6
CtR2$^g_{FeFe}$	-; 7123.1	8.1, 5.8 (2.1, 1.1)	7059.1
MmR2$^r_{FeFe}$	-; 7122.7	7.0, 8.6 (3.4, 3.3)	n.d.
Mn(IV/III); Fe(III)	6552.1/6549.7; 7122.7	n.d.	7058.9

3.4.2. EPR signals around g = 4

In all samples, EPR signals in the $g = 4$ region were observed. However, their spectral shapes differed (Fig. 4). The smallest signal of MmR2$^r_{FeFe}$ was likely due to minor amounts of "rhombic" high-spin Fe(III) ($S = 5/2$) [92], i.e. bound unspecifically or in single-occupancy R2 sites. In the Ct samples, larger signals of Fe(III) species were detected, showing pronounced line splitting only in metal-grown CtR2$^g_{MnFe}$, CtR1R2$^g_{MnFe}$, and CtR2$^g_{FeFe}$ (Fig. 4). In these samples also the Zn content was increased (Table 1). In agreement with EPR-simulations (not shown), the split $g = 4$ signal may be attributed to an Fe(III) weakly coupled to a Zn(II) in minor amounts of FeZn sites [93]. Contributions to the split signal from $S = 2$ Fe(II) species, however, cannot be fully excluded.

3.5. Fe and Mn K-edge XAS spectra

The XANES spectrum provides information on the metal oxidation state and first-sphere coordination [32,94]. The shape and energy of the Fe K-edge spectra of all RNR samples were rather similar (Fig. 5A). In comparison to Fe(III)$_2$O$_3$ this indicated the prevalence of Fe(III) in all proteins (Table 3). Spectral broadening at low edge energies suggested small Fe(II) contributions in CtR1R2$^g_{MnFe}$ and CtR1R2$^r_{FeFe}$ containing the R1R2 complex. A slightly higher edge energy in CtR1R2$^r_{FeFe}$ was likely due to the Fe(IV) contribution. The K-edge of MmR2$^r_{FeFe}$ showed an increased primary maximum, pointing to an overall more symmetric first-sphere iron coordination in the mouse R2 compared to the FeFe Ct R2.

More information on the Fe site symmetry and electronic structure was derived from the pre-edge features of high-resolution XANES spectra. These features are due to dipole-forbidden $1s \rightarrow 3d$ electronic transitions, which gain intensity, e.g., by $3d/4p$-orbital mixing upon decreasing symmetry of the iron coordination [95] (Fig. 5A, inset). Two major peak features in all spectra at ~7113.6 eV and ~7115.1 eV (Table 3) reflect $1s$ electron excitations into t_{2g} and e_g d-
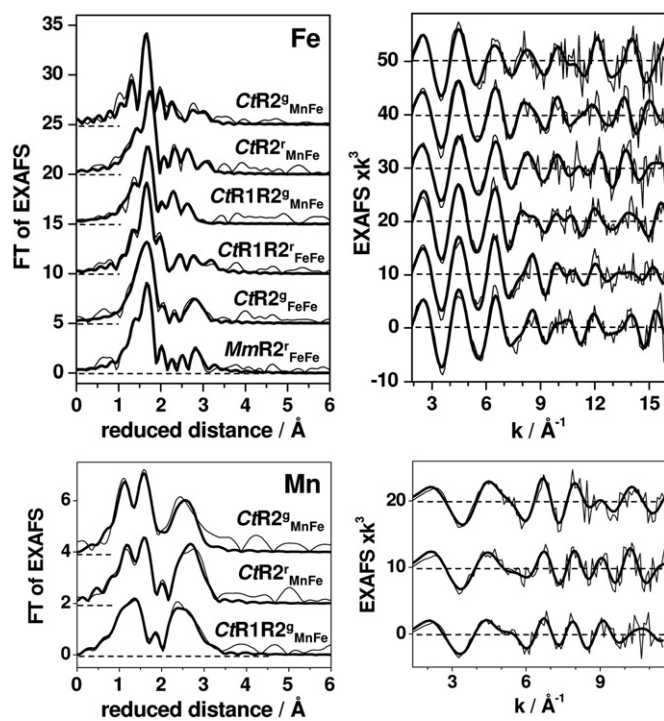
Fig. 6. EXAFS analysis of RNR proteins. Left panel, Fourier-transforms (FTs) of EXAFS spectra in the right panel (top, Fe spectra; bottom, Mn spectra). Thin lines, experimental data; thick lines, simulations with parameters in Table 4. FTs were calculated for k-ranges of 2–16 Å^{-1} (Fe) and 2–12 Å^{-1} (Mn) using cos^2-windows extending over 10% at both k-range ends.

orbitals [95]. The peak separation by ~1.5 eV is about the crystal field splitting energy (10*Dq*). It was similar to octahedral ferric model complexes with O and N ligands [95–97]. In *Ct*R2$^g_{FeFe}$ the ratio of the t_{2g} and e_g peak areas of ~1.4 (Table 3) was close to that for octahedral (O$_h$) Fe(III) [95,97]. For *Ct*R1R2$^r_{FeFe}$ additional spectral intensity at lower and higher energies suggests contributions from Fe(II) and Fe(IV) species (Table 3). The spectrum of *Mm*R2$^r_{FeFe}$ showed a smaller separation of its two main peaks, pointing to a deviation from centro-symmetry, i.e. due to a fraction of 5-coordinated Fe(III) [95].

In MnFe-containing *Ct*R2$^r_{MnFe}$ and *Ct*R1R2$^g_{MnFe}$, the e_g peak at higher energies was larger than the t_{2g} peak, at variance with *Ct*R2$^g_{MnFe}$ and FeFe-containing *Ct* samples for which this was reversed (Fig. 5A, Table 3). An enhanced e_g feature is observed for, e.g., 5-coordinated Fe(III), because axial bond elongation leads to enhanced $4pz/3dz^2$ orbital mixing with the $1s{\rightarrow}3dz^2$ transition at the highest energy [95]. Accordingly, this suggests longer (i.e. Fe–μOH instead of Fe–μO) or absent (5-coordinated iron) axial Fe–O bonds in *Ct*R2$^r_{MnFe}$ and *Ct*R1R2$^g_{MnFe}$ compared to *Ct*R2$^g_{MnFe}$. The latter sample thus presumably contained shorter Fe–μO bonds and 6-coordinated iron. A pre-edge feature at ~7117.8 eV in all samples (Fig. 5A) is assigned to $1s{\rightarrow}3d$ transitions due to inter-metal $4p/3d$ orbital mixing of the two metal ions [95,98]. This observation is in agreement with the short metal–metal distances in both the MnFe and FeFe sites (see later).

The Mn K-edge spectra are shown in Fig. 5B. The small pre-edge features of all samples suggest predominantly 6-coordinated Mn [57]. The edge energy of *Ct*R1R2$^g_{MnFe}$ was close to that of a Mn(III) reference (Table 3), in agreement with the large Mn(III)Fe(III) EPR signal in this sample. Mn(II) was almost absent as discernable from the first derivatives of K-edge spectra [32,99] (Fig. 5B). For both *Ct*R2$^g_{MnFe}$ and *Ct*R2$^r_{MnFe}$ the edge energy was closer to that of a Mn(IV) than to a Mn(III) reference (Table 3). This indicates that more than half of the manganese in these samples was present as Mn(IV).

3.6. EXAFS analysis

Interatomic distances in the metal sites were determined from EXAFS spectra at the Fe and Mn K-edges (Fig. 6). All Fourier-transformed (FT) spectra revealed maxima at 1–2 Å due to first-sphere ligands and at 2–3 Å mostly due to metal–metal distances. Gradual refinement of the fit approaches showed that highest fit qualities required three first-sphere metal–ligand distances and several metal–metal distances (Tables 4 and S1).

3.6.1. Fe-only containing samples

In *Ct*R2$^g_{FeFe}$ and *Mm*R2$^r_{FeFe}$ containing mainly Fe(III)Fe(III) cofactors, most Fe–O/N distances were around 2 Å and few shorter bonds of ~1.85 Å were detected (Table 4). The large Debye–Waller factor ($2\sigma^2$) of the ~2 Å O/N-shell suggests the presence of 5-coordinated
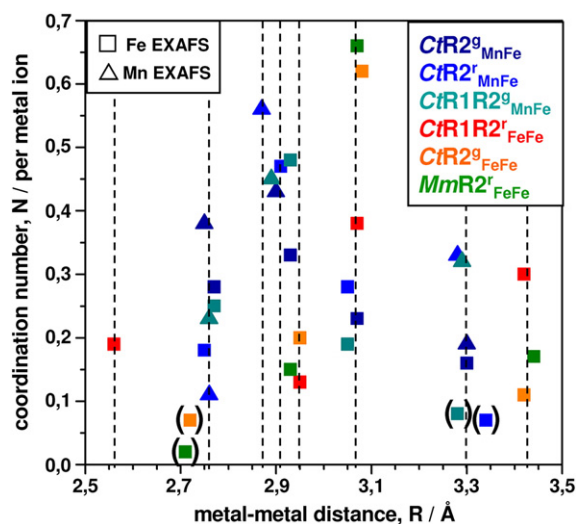

Fig. 7. Metal–metal distances in R2 proteins from EXAFS. Squares, data from Fe-EXAFS; triangles, data from Mn-EXAFS (see Table 4). Vertical dashed lines mark distances as discussed in the text. Small and presumably insignificant *N*-values are shown in parenthesis. For a similar graphical representation of respective first-sphere distances see Fig. S2.

iron besides the 6-coordinated iron. Fe–O/N distances of ~2.5 Å possibly reflect long Fe–N(His) bonds. The metal–metal distance in ~65% of both samples was 3.07 Å. This value hence reflects the major Fe(III)Fe(III) species, which is rather similar in *Ct* and *Mm* R2 (Fig. 7). Minor amounts of shorter (~2.95 Å) and longer (~3.4 Å) distances were likely due to a second Fe(III)Fe(III) species and to an Fe(III)Fe(II) state. In *Ct*R1R2$^r_{FeFe}$, higher numbers of short (~1.8 Å) and long (~2.2 Å) Fe–O/N bonds were detected compared to the *Ct* and *Mm* samples without R1 (Table 4). The shorter bonds should reflect Fe(IV)–μO motifs and the longer bonds Fe–N(His) interactions. Even shorter bonds, which could be due to Fe=O motifs, were absent. Only for *Ct*R1R2$^r_{FeFe}$, a particularly short Fe–Fe distance of 2.56 Å was found in ~20% of the protein (Fig. 7). We attribute it to an Fe(IV)Fe(III) site. Longer Fe–Fe distances of ~2.95 Å, ~3.05 Å, and ~3.4 Å as in *Ct*R1R2$^r_{FeFe}$ were also observed in the other Fe-only *Ct* and *Mm* R2 proteins (Fig. 7). They thus presumably belong to similar Fe(III)Fe(III) and Fe(III)Fe(II) sites present at varying concentrations in all these samples.

3.6.2. Mn and Fe containing samples

For the Mn,Fe containing proteins, both Fe and Mn EXAFS revealed that the first-sphere Fe–O/N and Mn–O/N distances were by at least 0.05 Å shorter in *Ct*R2$^g_{MnFe}$ compared to *Ct*R2$^r_{MnFe}$. The Mn–O/N
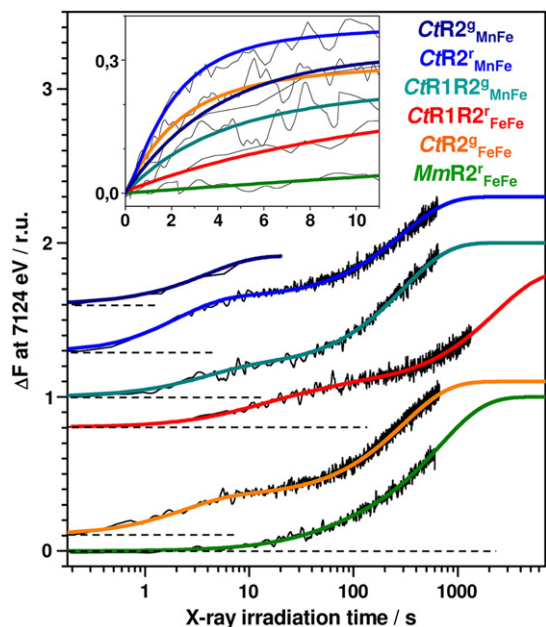
Table 4

Simulation parameters of Fe and Mn EXAFS spectra. Data sets correspond to fit curves shown in Fig. 6. N_i, coordination number; R_i, metal–ligand/metal distance; $2\sigma^2_i$, Debye–Waller factor; R_F, error sum calculated for reduced distances of 1–3.0 Å [57]. Fit restraints: the sum of *N*(O/N) values was set to 6, the sum of *N*(Fe/Mn–Fe) values was 1, $2\sigma^2_i$ was 0.002 Å^2 if not otherwise stated (see SI-2 for refinement of fit parameters for MnFe containing R2).

Sample	Metal–backscatterer interaction; N_i [per metal ion]/R_i [Å] ($2\sigma^2_i \times 10^3$ [Å^2])							R_F [%]
	Fe–O	Fe–O/N	Fe–O/N	Fe–Fe(Mn)	Fe–Fe(Mn)	Fe–Fe(Mn)	Fe–Fe(Mn)	
*Ct*R2$^g_{MnFe}$	0.81/1.77 (2)	4.10/1.98 (7)	1.09/2.18	0.28/2.77	0.33/2.93	0.23/3.07	0.16/3.30	15.8
*Ct*R2$^r_{MnFe}$	1.77/1.87 (9)	3.76/2.03 (5)	0.47/2.49	0.18/2.75	0.47/2.91	0.28/3.05	0.07/3.34	12.9
*Ct*R1R2$^g_{MnFe}$	0.60/1.78 (2)	4.87/1.99 (13)	0.53/2.46	0.25/2.76	0.48/2.92	0.19/3.05	0.08/3.28	17.4
*Ct*R1R2$^r_{FeFe}$	0.82/1.83 (2)	3.23/2.00 (4)	1.95/2.17	0.19/2.56	0.13/2.95	0.38/3.07	0.30/3.42	15.6
*Ct*R2$^g_{FeFe}$	0.44/1.87 (4)	4.90/2.01 (13)	0.66/2.52	0.07/2.72	0.20/2.95	0.62/3.08	0.11/3.42	14.5
*Mm*R2$^r_{FeFe}$	0.63/1.80 (2)	4.89/1.98 (10)	0.48/2.49	0.02/2.71	0.15/2.93	0.66/3.07	0.17/3.44	14.6
	Mn–O	Mn–O	Mn–O/N	Mn–Fe	Mn–Fe		Mn–Fe	
*Ct*R2$^g_{MnFe}$	0.87/1.71 (5)	4.35/1.91 (26)	0.78/2.38	0.38/2.75	0.43/2.90		0.19/3.30	10.1
*Ct*R2$^r_{MnFe}$	1.98/1.76 (20)	3.33/1.97 (25)	0.69/2.31	0.11/2.76	0.56/2.87		0.33/3.28	9.9
*Ct*R1R2$^g_{MnFe}$	1.78/1.78 (9)	2.88/2.00 (38)	1.34/2.18	0.23/2.76	0.45/2.89		0.32/3.29	8.1
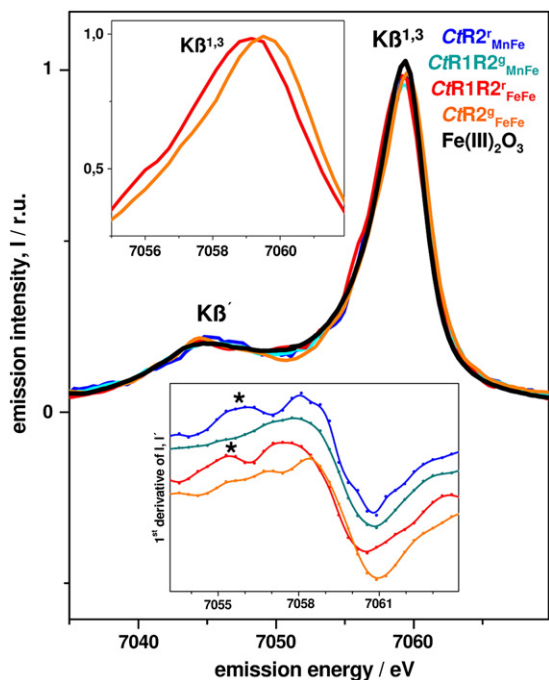
Fig. 8. Fe Kß X-ray emission line spectra of RNR. Spectra of proteins and of a powder sample of Fe(III)$_2$O$_3$ were normalized according to the areas under the curves. Upper inset, Kß^{1,3} lines in magnification; lower inset, first derivatives of spectra (asterisks mark additional maxima). Spectra represent averages of data measured on 3–5 sample spots.

distances in CtR2$^r_{MnFe}$ were more similar to those in CtR1R2$^g_{MnFe}$ (Table 4). Furthermore, the Mn–O/N bonds were by ~0.1 Å shorter than the Fe–O/N bonds, as expected for the higher mean Mn oxidation state in CtR2$^g_{MnFe}$ and CtR2$^r_{MnFe}$. Very short Mn–O bonds of

~1.7 Å were only detected in CtR2$^g_{MnFe}$, which likely are due to additional Mn(IV)–μO bonds. For CtR1R2$^g_{MnFe}$, the slightly longer mean Mn–ligand distance and the larger Debye–Waller factors of the major Fe,Mn–O interactions of ~2 Å suggested the presence of higher amounts of 5-coordinated metal ions.

A major metal–metal distance close to 2.9 Å and smaller amounts of distances of ~3.05 Å and ~3.3 Å were detected by Fe and Mn EXAFS in all three Mn,Fe-containing Ct R2 samples (Fig. 7). In CtR1R2$^g_{MnFe}$, the ~2.92 Å is the Mn(III)–Fe(III) distance, because this state was dominant according to EPR. The Mn(III)–Fe(III) distance hence was shorter than the distances attributed to Fe(III)Fe(III) sites (~2.95 Å, ~3.07 Å) in Fe-only R2. Notably, minor amounts of the ~3.07 Å distance were also detected by Fe EXAFS in the Mn,Fe Ct samples, meaning that these samples contained a similar Fe(III)Fe(III) state as the Fe-only samples. The longest distance of ~3.3 Å was similar to the ~3.4 Å of the Fe(III)Fe(II) state in the Fe-only R2 and hence attributed to small amounts of Mn(III)Fe(II) sites in the Mn,Fe-R2.

A particularly short metal–metal distance of ~2.75 Å was most prominent in the Fe and Mn EXAFS of CtR2$^g_{MnFe}$, present but less apparent for CtR1R2$^g_{MnFe}$, and close to the detection limit for CtR2$^r_{MnFe}$ (Fig. 7). A similar distance has been previously observed in Mn,Fe-grown Ct R2 and attributed to a Mn(IV)Fe(III) site [32]. The metal–metal distance of a second Mn(IV)Fe(III) site dominating in the Mn, Fe-reconstituted Ct R2 (CtR2$^r_{MnFe}$) was ~0.15 Å longer (2.91 Å) and similar to the Mn(III)Fe(III) site in CtR1R2$^g_{MnFe}$ (Fig. 7). The same value of 2.91 Å has previously been reported for reconstituted Ct R2 in the Mn(IV)Fe(III) state [45]. The Mn–Fe distance from Mn EXAFS, which was by ~0.04 Å shorter than the respective Fe–Mn distance from Fe EXAFS, and the Debye–Waller factor ($\sigma = 0.03$ Å, i.e. $2\sigma^2 = 0.002$ Å^2) suggested that in CtR2$^r_{MnFe}$ a minor fraction of Mn(IV)Mn(III) sites (see the EPR results) may have a Mn–Mn distance ≤2.84 Å.

3.7. Kß X-ray emission

The Kß X-ray emission lines reflect refilling of the 1s core hole by 3p electrons. Overlap of 3p and, e.g., 3d and valence electronic levels causes sensitivity of the line energy and shape to the metal oxidation state and coordination geometry [100,101]. The Fe Kß spectra of all samples overall were similar to Fe(III)$_2$O$_3$, indicating predominance of high-spin Fe(III) in the proteins (Fig. 8). The ~0.3 eV lower Kß^{1,3} line energy in CtR1R2$^r_{FeFe}$ presumably was explained by the admixture of ~20% Fe(IV) only in this sample [102–105]. The first-derivative spectra (Fig. 8) showed additional low-energy maxima for CtR2$^r_{MnFe}$ and CtR1R2$^r_{FeFe}$ compared to CtR1R2$^g_{MnFe}$ and CtR2$^g_{FeFe}$, due to shoulders on the Kß^{1,3} lines. Tentative multiplet calculations of Kß spectra [63] (not shown) revealed possible low-energy shoulders for increased coordination symmetry at Fe(III) or for an admixture of Fe(IV). This suggests octahedral Fe(III) in Mn(IV)Fe(III) sites of CtR2$^r_{MnFe}$ compared to, i.e., 5-coordinated Fe(III) in Mn(III)Fe(III) sites of CtR1R2$^g_{MnFe}$. CtR1R2$^r_{FeFe}$ likely contained near-octahedral Fe(IV).

Fig. 9. X-ray photoreduction of R2 metal sites at 20 K. Time-dependent changes of X-ray fluorescence levels (traces vertically displaced) due to shifts of the Fe K-edge to lower energies are shown (excitation energy of 7124 eV, detection of Kß fluorescence at 7059.5 eV; see SI-3). Black lines, experimental data (averages of 2–5 traces from individual sample spots); colored lines, simulations with parameters in Table 5; traces were normalized to unity total amplitude according to the fits. The time axes were corrected for slight variations in the incident X-ray flux (<10%) in measurements of the different samples, assuming a linear dependence of the photoreduction rate on the X-ray flux. Inset: the first seconds of traces on a linear time scale.

Table 5
Parameters describing X-ray photoreduction of iron in RNR samples. Halftimes and relative amplitudes (A) resulted from bi- or mono-exponential simulations of data in Fig. 9. [a]The amplitude of the fast phase for CtR2$^g_{MnFe}$ was estimated by comparison of its K-edges at 0 s and 30 s of irradiation to those of CtR2$^r_{MnFe}$ (slow phase not determined for CtR2$^g_{MnFe}$).

Sample	$t^1_{1/2}$ [s]	A^1 [%]	$t^2_{1/2}$ [s]	A^2 [%]
CtR2$^g_{MnFe}$	2.7	32[a]	n.d.	68[a]
CtR2$^r_{MnFe}$	1.8	38	253	62
CtR1R2$^g_{MnFe}$	2.2	19	201	81
CtR1R2$^r_{FeFe}$	13.7	34	231	66
CtR2$^g_{FeFe}$	1.6	25	209	75
MmR2$^r_{FeFe}$	–	–	299	100
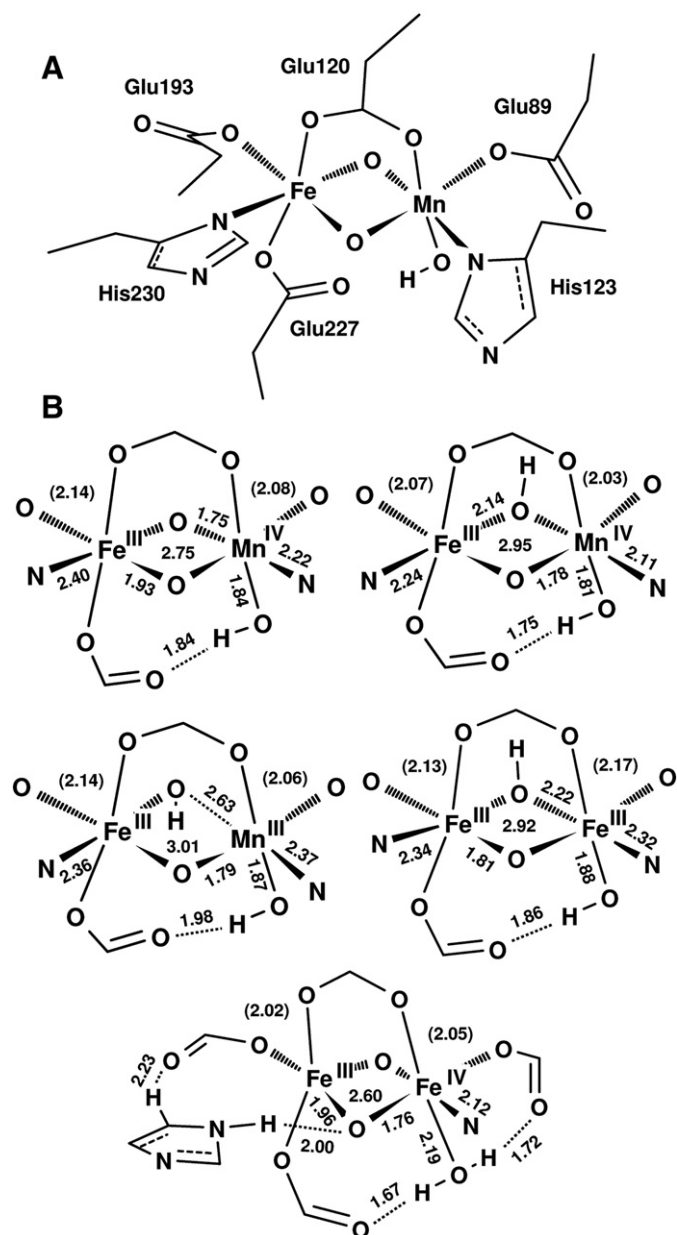
Fig. 10. Model structures of metal sites in R2 from DFT calculations. (A) Structure with amino acid metal–ligands derived from *Ct* R2 crystal data (1SYY) and used as a starting point for DFT (for atomic coordinates of the respective FeFe and MnFe structures see Table S2). (B) Core structures from DFT for two Mn(IV)Fe(III) species (top), Mn(III)Fe(III) (middle left) and Fe(III)Fe(III) (middle right) sites, and an example of an Fe(IV)Fe(III) site with 5-coordinated Fe(III), additional H-bonding, and shorter Fe–Fe distance (bottom). Metal distances and selected bond lengths, i.e. longest and shortest Fe,Mn–$\mu O(H_n)$ bonds, are given in Å (mean Fe–O distances in parenthesis). For further model structures see Fig. S4.

3.8. X-ray photoreduction and redox potentials

X-ray induced reduction of iron was monitored by shifts of the Fe K-edge to lower energies [38,56] (Figs. 9 and S3). The slow monophasic reduction of $MmR2^r_{FeFe}$ likely reflected the Fe(III)Fe(III)→Fe(III)Fe(II) transition. The second Fe(III) seemingly was not reduced on the experimental time scale. The *Ct* RNR samples showed biphasic photoreduction with halftimes of a few seconds and several minutes both for MnFe and FeFe containing R2 (Table 5) (Fig. 9). For $CtR2^g_{FeFe}$ the two phases may be due to the reduction of two different Fe(III)Fe(III) sites, correlating to the minor (~2.95 Å) and major (~3.07 Å) Fe(III)–Fe(III) distances. The major slower phase may belong to an Fe(III)Fe(III) site

similar to the one in $MmR2^r_{FeFe}$. For $CtR1R2^r_{FeFe}$ the first reduction phase was considerably slower than for $CtR2^g_{FeFe}$ (Table 5). Its small magnitude suggested assignment to the Fe(IV)Fe(III) state in ~20% of the protein. $CtR2^g_{MnFe}$, $CtR2^r_{MnFe}$, and $CtR1R2^g_{MnFe}$ showed similar biphasic reduction kinetics as $CtR2^g_{FeFe}$. The fast phase was larger in $CtR2^g_{MnFe}$ and $CtR2^r_{MnFe}$ compared to $CtR1R2^g_{MnFe}$, in agreement with the higher Mn(IV) content in the former samples. It thus was attributed to reduction of Fe(III) in Mn(IV)Fe(III) sites. The slower phase was assigned to reduction of Fe(III) in Mn(III)Fe(III) and Fe(III)Fe(III) sites present in all three Mn,Fe-containing R2 samples.

Faster X-ray reduction was expected for a more positive redox midpoint potential (E_m) of the metal sites [56,106]. Thus, the respective halftimes (Table 5) suggest the following order of E_m values: Mn(IV)Fe(III) reconstituted ≈ Fe(III)Fe(III) (high-E_m species) ≥ Mn(IV)Fe(III) grown > Fe(IV)Fe(III) > Mn(III)Fe(III) and Fe(III)Fe(III) (low-E_m species) >> Fe(III)Fe(II). The Mn(IV)Fe(III) states were similarly rapidly reduced as the water-oxidizing manganese complex of photosystem II possessing an E_m close to +1 V [38,107,108]. The Mn(IV)Fe(III) sites in R2 thus likely exhibit a comparably positive redox potential.

3.9. Density functional theory calculations

Geometry-optimizations using DFT were carried out on MnFe and FeFe site models to verify structural and electronic features deduced from the spectroscopic data (Fig. 10). A classical "diamond" core geometry, featuring a Mn(IV)$(\mu O)_2$Fe(III) site with one carboxylate bridge, readily reproduced the ~2.75 Å metal–metal distance particularly observed for $CtR2^g_{MnFe}$, in agreement with previous DFT results [30,45,109]. Also the Mn/Fe-N(His) and mean Mn/Fe-O(Glu) distances and a particularly short Mn(IV)–μO bond were in good agreement with the EXAFS data (Fig. 10). Protonation of one bridging oxide in a Mn(IV)$(\mu O)(\mu OH)$Fe(III) core elongated the metal–metal distance to 2.95 Å. This distance is similar to the main Mn(IV)–Fe(III) distance in $CtR2^r_{MnFe}$. For the protonated bridge, a homogenization of Fe–ligand bond lengths was observed in the DFT structure, which also is in agreement with the EXAFS analysis.

For both Mn(III)Fe(III) and Fe(III)Fe(III) sites, metal–metal distances close to the ~3 Å found in the RNR samples were calculated for $(\mu O)(\mu OH)$-bridged complexes (Fig. 10) [30,45,109]. However, depending on the particular combination of bridging $\mu O/\mu OH$ and terminal OH/OH_2 groups, also deviating Mn/Fe(III)Fe(III) structures with distances in the range of about 2.6–3.0 Å were obtained (for an example see Fig. S4). As a tendency, the shorter distances required more severe structural changes in the complex, e.g. 5-coordinated Fe(III) or Mn(III), and more extensive hydrogen bonding [109].

The short metal–metal distance of 2.56 Å, attributed to the Fe(IV)Fe(III) site in $CtR1R2^r_{FeFe}$, seemingly did not reflect a canonical "diamond" core. The DFT structure of an Fe(IV)$(\mu O)_2$Fe(III) site showed a 2.72 Å distance, similar to the Mn(IV)Fe(III) site [30,86,110]. However, there was a trend in the calculations that the Fe(III) became 5-coordinated by histidine ligand rotation, inducing more complex H-bonding patterns, which involved terminal OH_n ligands at the Fe(IV) and carboxyl side chains. Such a structure produced an Fe(IV)–Fe(III) distance of 2.6 Å (Figs. 10 and S4). Notably, structures containing Fe(IV)Fe(III) and bridging-chelating carboxylates [32] or a triple-$\mu O(H)$ bridge [111] were unstable in the DFT calculations and transformed into $\mu O(H)_2$-bridged structures (not shown) with metal–metal distances exceeding 2.7 Å.

The electronic configurations from DFT for the two different Mn(IV)Fe(III) sites (Fig. 10) indicated high-spin octahedral Fe(III) (about equal occupancy of the 5*d*-orbitals) and high-spin octahedral Mn(IV) (equal occupancy of low-energy t_{2g} (xy, xz, yz) and lower occupancy of higher energy e_g (x^2-y^2, z^2) *d*-orbitals). The dz^2 orbitals approximately aligned along the opposed Mn–$\mu O(H)$ and Fe–μO bonds in the structures (Fig. 11). The more localized Mn dz^2 orbital and by ~1.5 eV lower *d*-orbital energies of Mn and Fe in the
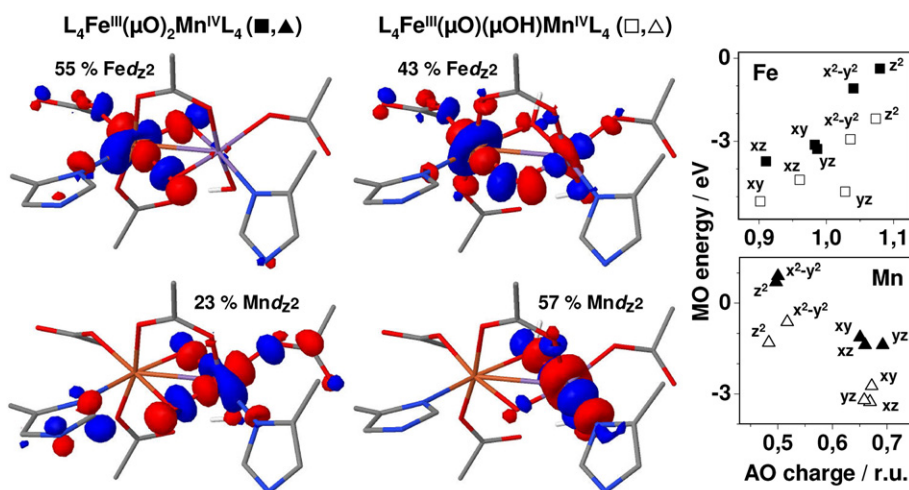
Fig. 11. Electronic configuration of Mn(IV)Fe(III) sites from DFT (see Fig. 10). Left: molecular orbitals (MOs) with highest metal-dz^2 character aligning with metal–μO(H) bonds. Right: metal-d atomic orbital (AO) charges (normalized to sums of 3 for Mn(IV) and 5 for Fe(III)) versus averaged energies of α- and ß-spin MOs with highest respective Fe-d contents.

Mn(IV)(μO)(μOH)Fe(III) site (Fig. 11) suggest a higher redox potential of the protonated Mn(IV)Fe(III) site. By ~4 eV lower d-orbital energies of Fe(III) compared to Mn(IV) implied that reduction of the Fe(III) ion should precede the reduction of the Mn(IV) [32].

4. Discussion

### 4.1. Tentative assignment of metal cofactor species

The spectroscopic data in the present work and in previous studies [2,12,13,32,45,77] provide evidence for at least ten different metal site species of the MnFe and FeFe types in the *Ct* R2 protein. For the higher valence states, the structural features of the metal sites seem to deviate significantly from crystal data of R2 proteins (Fig. 1). Tentatively, we assign the states found in *Ct* R2, particularly relying on the metal–metal distance, as follows: Fe(IV)Fe(III), ~2.55 Å; Mn(IV)Fe(III), ~2.75 Å and ~2.90 Å; Mn(III)Fe(III), ~2.90 Å; Fe(III)Fe(III), ~2.95 Å and ~3.07 Å; Mn(III)Fe(II), ~3.30 Å; Fe(III)Fe(II), ~3.42 Å. A Mn(IV)Mn(III) site found in low amounts may correspond to a ~2.85 Å distance. In a previous XAS study, a metal–metal distance of ~3.65 Å was attributed to a Mn(III)Fe(II) site, possibly containing a

bridging-chelating carboxyl group, and a distance of ~4.15 Å was assigned to a Mn(II)Fe(II) site [32].

The five more prominent metal cofactor species are related to the presently studied RNR samples as derived by the various procedures for metal incorporation and oxidation in Fig. 12. Because of their relatively high abundance in one or several samples and/or due to their more distinct structural and spectroscopic features, these respective species appear to be relatively clearly defined (see below). We note that in particular the longest metal–metal distances, which were found in minor quantities in the R2 proteins, may in part also reflect the presence of differently metallated sites such as Fe/Mn–Zn(II)/Cu(II) species. However, the metal–metal distances shorter than ~3 Å, which most likely require di-μO(H)-bridging of metal ions with valences of (III) or (IV), in our opinion are unlikely to be due to sites containing divalent Zn or Cu ions.

4.2. Heterogeneity of metal sites in the RNR samples

To access a broad range of different metal site configurations, we have prepared the R2 protein samples according to procedures, which have been established previously in the literature [2,12,13,32,45,77]. The metal ions either were incorporated *in vivo*
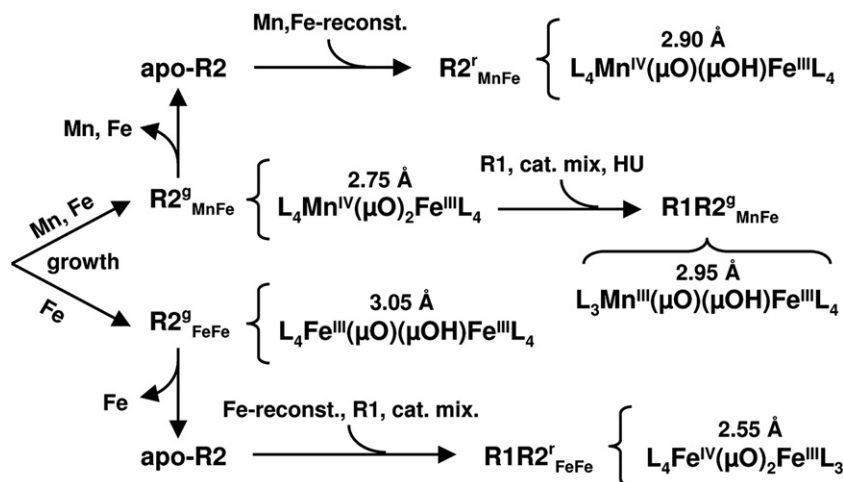
Fig. 12. *Ct* RNR protein preparations and prominent metal site species in R2. Further species exist in all samples (see the text). L = terminal metal–ligands (carboxyls of Glu, OH$_n$, possibly peroxidic species in certain metal(III)$_2$ states), cat. mix. = catalytic mixture, HU = hydroxyurea; respective rounded metal–metal distances and valences are indicated. Bridging motifs (μO(H)) and ligand numbers are tentative, but plausible according to XAS and DFT.

(as-grown R2 overexpressed in *E. coli*) or *in vitro* (metal-reconstituted R2 apo-protein). The metal cofactor configuration of R2 in the afterwards deep-frozen protein samples thus is expected to represent a "snapshot" of the various steps of the oxygen activation reaction performed by the R2 protein and/or of the catalytic reactions occurring in the R1R2 complex. Metal site heterogeneity therefore is an intrinsic feature of these samples. A study of the pure states presumably would require a protocol for reaction synchronization, which presently is not yet available. However, by the applied multi-spectroscopy approach, including XAS/XES, EPR, and optical absorption and Raman spectroscopy methods, the various site characteristics, as based on different electronic and structural features, at least in part, were resolvable.

4.3. Properties of an Fe(IV)Fe(III) cofactor in Ct R2

Only in the *Ct* R1R2 complex containing an FeFe site in R2 and after catalytic turnover in the presence of nucleotides, a particular state was detected that we assign to an Fe(IV)Fe(III) species. This species apparently is distinguished by a specific EPR spectrum [29,36,91], optical absorption and Raman features, and XAS/XES signatures. Its very short metal–metal distance of ~2.55 Å is quite unusual. However, similar distances have been detected for R2 of other RNRs and also for methane-monooxygenase (MMO), which contains a comparable metal site [112]. In the latter studies, the short distance consistently has been assigned to Fe(IV)Fe(III) states [48,49,113]. The optical absorption spectrum of the *Ct* R2 is very similar to synthetic Fe(IV)Fe(III) compounds, for which the absorption maximum around 650 nm was assigned to ligand-to-metal or, perhaps more likely, metal-to-metal charge transfer bands [78–80]. A prominent Raman band at ~395 cm^{-1} of the *Ct* R2 is not yet assigned unambiguously, but at the lower frequency limit for Fe–μO vibrations in model compounds [80–82]. This cumulative evidence favors the presence of a distinct Fe(IV)Fe(III) species in *Ct*R1R2$^{r}_{FeFe}$.

The Fe(IV)Fe(III) state has been denoted "intermediate *X*" and this species is believed to oxidize the nearby tyrosine in class Ia R2 proteins [35,36]. Structural proposals for this state include typical "diamond" cores (L$_4$Fe(IV)(μO)(μO(H))Fe(III)L$_4$, L represents non-bridging ligands) [1,30,36,114–116], but also more distorted site geometries, which in some cases contain a bridging-chelating carboxyl side chain [29,117]. For the Fe(IV)Fe(III) site in *Ct* R2, our DFT and XAS results suggest that a short Fe-Fe distance requires considerable asymmetry at the two iron atoms, which possibly may be achieved by the presence of one 5-coordinated Fe(III) and by additional hydrogen-bonding between OH$_n$–ligands and carboxyl groups for example (Fig. 10). Interestingly, the slower X-ray photoreduction suggested a lower apparent redox potential (E_m) of the Fe(IV)Fe(III) site compared to the Mn(IV)Fe(III) sites. This result is in contrast to DFT calculations in Ref. [30], which suggest that the Fe(IV)Fe(III) cofactor is a stronger oxidant than the Mn(IV)Fe(III) cofactor. However, our spectroscopic results suggest that the "green" Fe(IV)Fe(III) cofactor exhibits a different ligand geometry than the "diamond core" structure considered in Ref. [30], which may account for its lower E_m. The lower E_m of this Fe(IV)Fe(III) species in the tyrosine-lacking R2 of *Ct* RNR may relate to the inferior activity of the FeFe cofactor compared to the MnFe cofactor in initiating the reversible redox cascade in the R1 subunit [37,118,119].

4.4. Two configurations of the Mn(IV)Fe(III) site in Ct R2

The X-ray spectroscopy results on the metal-reconstituted and -grown Mn(IV)Fe(III)-containing *Ct* R2 proteins, in particular the by ~0.15 Å longer Mn–Fe distance, the more symmetric Fe(III) coordination, and the slightly faster X-ray reduction of the Fe(III) in *Ct*R2$^{r}_{MnFe}$ compared to *Ct*R2$^{g}_{MnFe}$, strongly suggest that two different configurations of the Mn(IV)Fe(III) cofactor can exist in this enzyme. For the
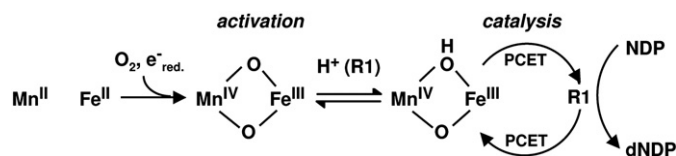
Fig. 13. Activation and catalysis in MnFe RNR. Starting from the Mn(II)Fe(II) state, activation by O_2 should involve three-fold metal oxidation and one electron from an external reductant (red.) [1,2], to reach a Mn(IV)(μO)$_2$Fe(III) "diamond" core structure of the metal cofactor in R2. The protonated Mn(IV)(μO)(μOH)Fe(III) site, due to its more positive E_m, supposedly initiates the redox cascade in R1 involving forward and reverse long-range proton-coupled electron transfer (PCET) between the metal site in R2 and the active site in R1 during cysteine radical formation and ribonucleotide-diphosphate (NDP) reduction and conversion to deoxyribonucleotide-diphosphate (dNDP) [22]. Inter-conversion of the two Mn(IV)Fe(III) states could result, e.g., from a structural change in R2 leading to (reversible) μO-bridge protonation, and may even be related to the binding of R1.

reconstituted *Ct* R2, the Mn–Fe distance of ~2.90 Å is similar to that in a previous report [45] and we thus attribute it to the same Mn(IV)Fe(III) species described in Ref. [45]. For the metal-grown R2, besides a ~2.90 Å distance, we have found an additional Mn–Fe distance of ~2.75 Å in this work and previously in similar samples [32]. These results and our DFT calculations on Mn(IV)Fe(III) model structures are consistently explained under the assumption, that the ~2.75 Å distance belongs to a second type of Mn(IV)Fe(III) cofactor. The prevailing Mn(IV)Fe(III) species thus seems to depend on the procedure, which is used for the assembly of the metal cofactor in *Ct* R2. The model structures from DFT in the present study and in previous reports [30,36,109] suggest that a L$_4$Mn(IV)(μO)$_2$Fe(III)L$_4$ "diamond" core structure readily accounts for the ~2.75 Å distance in the metal-grown R2 (Fig. 12).

As implied by the DFT results in this work and from other authors, already a slight modification, namely a single protonation of a bridging oxide to yield a (μO)(μOH) motif, can explain the metal distance elongation and homogenization of the Fe(III) bond lengths observed in the Mn,Fe-reconstituted *Ct* R2 [30,36,109]. Such a deviating protonation state may be related to differences in the site assembly sequence in the cell and during the reconstitution procedure. This may lead to a different H-bonding network around the cofactor, for example due to varying numbers or orientations of nearby water molecules, which may result in a shift of the pK of a bridging oxide [119].

At least catalytic turnover in the R1R2 complex seems to involve similar MnFe site species in R2, independently of the metal site assembly procedure. Evidence for this conclusion comes from the observation by EPR of a similar hydroxyurea-inhibited Mn(III)Fe(III) state in both Mn,Fe-grown and Mn,Fe-reconstituted R2 in the presence of R1 [13,32,77,88]. Because this Mn(III)Fe(III) state apparently is the reduction product of a Mn(IV)Fe(III) precursor, this could mean that also the precursor is similar in both protein types. Possibly, the protonation state of the oxo-bridge may even be related to a conformational change due to R1 binding. Thus, both Mn(IV)Fe(III) states could be viable intermediates in the O_2-activation process of R2. Our X-ray photoreduction study showed a slightly faster reduction of the Fe(III) in the Mn(IV)Fe(III) site of the Mn,Fe-reconstituted compared to the Mn,Fe-grown *Ct* R2. We interpret this result as an indication for a higher apparent E_m in the reconstituted protein. Therefore, presumably the Mn(IV)(μO)(μOH)Fe(III) species initiates the redox cascade in R1 [119]. It is tempting to speculate that R2 site protonation related to R1 binding could even be a regulatory process, which prevents premature reduction of the metal cofactor prior to catalysis in R1 in the cell (Fig. 13).

4.5. X-ray photoreduction of the metal cofactors

Additional configurations of the metal cofactor were observed in all R2 samples. Evidence for minor amounts of a Mn(IV)Mn(III) site

in Mn,Fe-reconstituted *Ct* R2 was obtained by EPR and XAS, tentatively assigned to a Mn–Mn distance of ~2.85 Å in a Mn(IV)(μOH$_n$)$_2$Mn(III) bridged complex. This is not surprising because crystal structures show that MnMn sites in R2 are stable species [120–123]. That such MnMn sites may also be active in the O$_2$-activation chemistry is implied by their apparent high-valence state. The lack of evidence for MnMn species in the metal-grown *Ct* R2 could suggest that *in vivo* mechanisms exist for the discrimination of Mn and Fe ions during insertion into their specific binding positions in R2.

Several different configurations of metal(III)$_2$ species could be discriminated. An Fe(III)Fe(III) site with a metal–metal distance of ~3.07 Å was found in the R2 proteins from both *Ct* and *Mm*. This could mean that the overall cofactor structure is similar and insensitive to the exchange of an Asp for a Glu residue as a metal–ligand in *Ct* R2. Similarly rapid X-ray photoreduction suggests that also the E_m of both species is similar. The photoreduction velocity of a minor FeFe species (metal–metal distance of ~2.95 Å) in the Fe-grown *Ct* R2 was close to that of the Mn(IV)Fe(III) sites. Because there was no evidence for Fe(IV) in this sample, it is assigned to an Fe(III)Fe(III) state, which may comprise a 5-coordinated Fe(III). The Mn–Fe distance for the as-grown Mn(III)Fe(III) site was ~2.90 Å, similar to the Mn(IV)Fe(III) site in the metal-reconstituted *Ct* R2. The slower photoreduction, however, suggested a considerably lower E_m for the Mn(III)-containing site. According to our XAS and DFT results, the Mn(III)Fe(III) site may contain a 5-coordinated Mn(III), as also proposed, e.g., for Mn(III) in the manganese complex of photosystem II [43].

The longest metal–metal distance of ~3.4 Å detected by XAS is similar to the distances that usually were observed in crystallized *Ct* FeFe R2 (Fig. 1). Fe(III)Zn(II) sites also show a similar metal–metal distance [124]. The assignment of the ~3.4 Å distance to an Fe(III)Fe(II) site is in agreement with a previous proposal [32]. A slightly shorter (~3.3 Å) distance is attributed to a Mn(III)Fe(II) site, which possibly contains a 5-coordinated Mn(III) ion. Comparison of the metal–metal distances of the Mn/Fe(III)Fe/Zn(II) sites with the diffraction data suggests that eventually in all crystal structures of R2 at least one divalent metal ion is present (Fig. 1). X-ray photoreduction within seconds of the Mn(IV)- and Fe(IV)-containing cofactors and even of an Fe(III)Fe(III) site at a temperature as low as 20 K in the XAS experiments suggests an E_m close to $+1$ V for these species [38,56]. Therefore, we conclude that X-ray induced reduction of higher valence states of the metal cofactor in R2 is difficult to avoid during crystallographic data collection, which usually involves higher X-ray doses and temperatures, as it is for other high-valent metal cofactors in proteins [38,56,125].

4.6. Mechanistic considerations

In previous studies on the *Ct* RNR lacking the radical-forming tyrosine, reaction sequences have been proposed for O$_2$ activation, leading to high-valent metal cofactors in R2 and subsequent radical formation in R1, which involve, e.g., metal-bound peroxidic species [32,51,119]. Bridging or end-on peroxides also may account for certain metal–ligand bond lengths of the Mn/Fe(III)Fe(III) states as determined in the present study. However, OOH$_n$ ligands cannot be discriminated from OH$_n$ ligands solely on the basis of XAS data. Further Raman studies on *Ct* R2 are required to clarify this important issue.

Consistently, Mn(IV)Fe(III) states in *Ct* R2 have been suggested to functionally substitute the Y•-Fe(III)Fe(III) entity in conventional R2 proteins during ribonucleotide reduction [1,2,12,109]. We propose that both detected Mn(IV)Fe(III) site configurations may be involved in O$_2$-activation by the *Ct* R2. Presumably, it is the protonated cofactor possessing a somewhat higher apparent E_m, which initiates the reversible proton-coupled electron-transfer (PCET) reactions in R1 during ribonucleotide reduction (Fig. 13). Our DFT results, showing that the Mn dz^2 orbital is more condensed and oriented in the direction

of the Mn-His123 bond for the protonated structure, support the hypothesis, previously put forward by Bollinger et al. [126], that the Mn ion is the entry point for electron transfer along the Trp51-Asp226-His123 hydrogen-bonded amino acid cluster to the metal site in *Ct* R2.

Clearly, further investigations are required to unravel the complete molecular structure and functional significance of all relevant configurations of MnFe and FeFe cofactors in RNR catalysis. However, the cumulative spectroscopic evidence presented here widens the concept of metal cluster structures in electron transfer enzymes such as RNR. It reveals a manifold of ligation environments in the different redox states of a dedicated metal site, which may even depend on inter-subunit interactions in the course of the enzyme reaction.

Appendix A. Supplementary data

Supplementary data to this article can be found online at doi:10.1016/j.bbabio.2011.12.008.

References

[1] J.A. Cotruvo Jr., J. Stubbe, Class I ribonucleotide reductases: metallocofactor assembly and repair *in vitro* and *in vivo*, Annu. Rev. Biochem. 80 (2011) 19.11–19.35.

[2] J.M. Bollinger Jr., W. Jiang, M.T. Green, C. Krebs, The manganese(IV)/iron(III) cofactor of *Chlamydia trachomatis* ribonucleotide reductase: structure, assembly, radical initiation, and evolution, Curr. Opin. Struct. Biol. 18 (2008) 650–657.

[3] M. Högbom, Metal use in ribonucleotide reductase R2, di-iron, di-manganese and heterodinuclear—an intricate bioinorganic workaround to use different metals for the same reaction, Metallomics 3 (2011) 110–120.

[4] B.M. Sjöberg, A. Gräslund, Ribonucleotide reductase, Adv. Inorg. Biochem. 5 (1983) 87–110.

[5] P. Nordlund, P. Reichard, Ribonucleotide reductases, Annu. Rev. Biochem. 75 (2006) 681–706.

[6] J. Herrick, B. Sclavi, Ribonucleotide reductase and the regulation of DNA replication: an old story and an ancient heritage, Mol. Microbiol. 63 (2007) 22–34.

[7] E. Torrents, P. Aloy, I. Gibert, F. Rodriguez-Trelles, Ribonucleotide reductases: divergent evolution of an ancient enzyme, J. Mol. Evol. 55 (2002) 138–152.

[8] S.J. Elledge, Z. Zhou, J.B. Allen, Ribonucleotide reductase: regulation, regulation, regulation, Trends Biochem. Sci. 17 (1992) 119–123.

[9] G. Bunker, L. Petersson, B.M. Sjöberg, M. Sahlin, M. Chance, B. Chance, A. Ehrenberg, Extended x-ray absorption fine structure studies on the iron-containing subunit of ribonucleotide reductase from *Escherichia coli*, Biochemistry 26 (1987) 4708–4716.

[10] R.S. Stephens, S. Kalman, C. Lammel, J. Fan, R. Marathe, L. Aravind, W. Mitchell, L. Olinger, R.L. Tatusov, Q. Zhao, E.V. Koonin, R.W. Davis, Genome sequence of an obligate intracellular pathogen of humans: *Chlamydia trachomatis*, Science 282 (1998) 754–759.

[11] C. Roshick, E.R. Iliffe-Lee, G. McClarty, Cloning and characterization of ribonucleotide reductase from *Chlamydia trachomatis*, J. Biol. Chem. 275 (2000) 38111–38119.

[12] M. Högbom, P. Stenmark, N. Voevodskaya, G. McClarty, A. Gräslund, P. Nordlund, The radical site in chlamydial ribonucleotide reductase defines a new R2 subclass, Science 305 (2004) 245–248.

[13] W. Jiang, D. Yun, L. Saleh, E.W. Barr, G. Xing, L.M. Hoffart, M.A. Maslak, C. Krebs, J.M. Bollinger Jr., A manganese(IV)/iron(III) cofactor in *Chlamydia trachomatis* ribonucleotide reductase, Science 316 (2007) 1188–1191.

[14] N. Voevodskaya, A.J. Narvaez, V. Domkin, E. Torrents, L. Thelander, A. Gräslund, Chlamydial ribonucleotide reductase: Tyrosyl radical function in catalysis

replaced by the FeIII–FeIV cluster, Proc. Natl. Acad. Sci. U. S. A. 103 (2006) 9850–9854.

[15] G. Schenk, C.L. Boutchard, L.E. Carrington, C.J. Noble, B. Moubaraki, K.S. Murray, J. de Jersey, G.R. Hanson, S. Hamilton, A purple acid phosphatase from sweet pota- to contains an antiferromagnetically coupled binuclear Fe–Mn center, J. Biol. Chem. 276 (2001) 19084–19088.

[16] C. Krebs, M.L. Matthews, W. Jiang, J.M. Bollinger Jr., AurF from *Streptomyces thio- luteus* and a possible new family of manganese/iron oxygenases, Biochemistry 46 (2007) 10413–10418.

[17] C.S. Andersson, M. Högbom, A *Mycobacterium tuberculosis* ligand-binding Mn/Fe protein reveals a new cofactor in a remodeled R2-protein scaffold, Proc. Natl. Acad. Sci. U. S. A. 106 (2009) 5633–5638.

[18] M. Högbom, The manganese/iron-carboxylate proteins: what is what, where are they, and what can the sequences tell us? J. Biol. Inorg. Chem. 15 (2010) 339–349.

[19] P. Nordlund, H. Eklund, Structure and function of the *Escherichia coli* ribonucle- otide reductase protein R2, J. Mol. Biol. 232 (1993) 123–164.

[20] D.T. Logan, X.D. Su, A. Aberg, K. Regnström, J. Hajdu, H. Eklund, P. Nordlund, Crystal structure of reduced protein R2 of ribonucleotide reductase: the struc- tural basis for oxygen activation at a dinuclear iron site, Structure 4 (1996) 1053–1064.

[21] J. Stubbe, P. Riggs-Gelasco, Harnessing free radicals: formation and function of the tyrosyl radical in ribonucleotide reductase, Trends Biochem. Sci. 23 (1998) 438–443.

[22] S.Y. Reece, J.M. Hodgkiss, J. Stubbe, D.G. Nocera, Proton-coupled electron trans- fer: the mechanistic underpinning for radical transport and catalysis in biology, Philos. Trans. R. Soc. Lond. B Biol. Sci. 361 (2006) 1351–1364.

[23] A. Adrait, M. Öhrström, A.L. Barra, L. Thelander, A. Gräslund, EPR studies on a sta- ble sulfinyl radical observed in the iron-oxygen-reconstituted Y177F/I263C pro- tein R2 double mutant of ribonucleotide reductase from mouse, Biochemistry 41 (2002) 6510–6516.

[24] S. Licht, G.J. Gerfen, J. Stubbe, Thiyl radicals in ribonucleotide reductases, Science 271 (1996) 477–481.

[25] S.S. Mao, T.P. Holler, G.X. Yu, J.M. Bollinger Jr., S. Booker, M.I. Johnston, J. Stubbe, A model for the role of multiple cysteine residues involved in ribonucleotide reduc- tion: amazing and still confusing, Biochemistry 31 (1992) 9733–9743.

[26] W.A. Prinz, F. Åslund, A. Holmgren, J. Beckwith, The role of the thioredoxin and glutaredoxin pathways in reducing protein disulfide bonds in the *Escherichia coli* cytoplasm, J. Biol. Chem. 272 (1997) 15661–15667.

[27] M. Bennati, F. Lendzian, M. Schmittel, H. Zipse, Spectroscopic and theoretical ap- proaches for studying radical reactions in class I ribonucleotide reductase, Biol. Chem. 386 (2005) 1007–1022.

[28] A. Larsson, B.M. Sjöberg, Identification of the stable free radical tyrosine residue in ribonucleotide reductase, EMBO J. 5 (1986) 2037–2040.

[29] N. Voevodskaya, M. Galander, M. Högbom, P. Stenmark, G. McClarty, A. Gräslund, F. Lendzian, Structure of the high-valent Fe^{III}Fe^{IV} state in ribonucleotide reduc- tase (RNR) of *Chlamydia trachomatis*—Combined EPR, ^{57}Fe-, ^{1}H-ENDOR and X-ray studies, Biochim. Biophys. Acta 1774 (2007) 1254–1263;
C.S. Andersson, M. Öhrström, A. Popovic-Bijelic, A. Gräslund, P. Stenmark, M. Högbom, The manganese ion of the heterodinuclear Mn/Fe cofactor in *Chlamydia trachomatis* ribonucleotide reductase R2c is located at metal position 1, J. Am. Chem. Soc. (2012), doi:10.1021/ja209678x.

[30] K. Roos, P.E. Siegbahn, Density functional theory study of the manganese- containing ribonucleotide reductase from *Chlamydia trachomatis*: why manga- nese is needed in the active complex, Biochemistry 48 (2009) 1878–1887.

[31] J.A. Cotruvo Jr., J. Stubbe, An active dimanganese(III)-tyrosyl radical cofactor in *Escherichia coli* class Ib ribonucleotide reductase, Biochemistry 49 (2010) 1297–1309.

[32] N. Voevodskaya, F. Lendzian, O. Sanganas, A. Grundmeier, A. Gräslund, M. Haumann, Redox intermediates of the Mn–Fe site in subunit R2 of *Chlamydia trachomatis* ribonucleotide reductase: an X-ray absorption and EPR study, J. Biol. Chem. 284 (2009) 4555–4566.

[33] L. Saleh, C. Krebs, B.A. Ley, S. Naik, B.H. Huynh, J.M. Bollinger Jr., Use of a chem- ical trigger for electron transfer to characterize a precursor to cluster X in as- sembly of the iron-radical cofactor of *Escherichia coli* ribonucleotide reductase, Biochemistry 43 (2004) 5953–5964.

[34] A. Gräslund, M. Sahlin, Electron paramagnetic resonance and nuclear magnetic resonance studies of class I ribonucleotide reductase, Annu. Rev. Biophys. Bio- mol. Struct. 25 (1996) 259–286.

[35] W. Tong, D. Burdi, P. Riggs-Gelasco, S. Chen, D. Edmondson, B.H. Huynh, J. Stubbe, S. Han, A. Arvai, J. Tainer, Characterization of Y122F R2 of *Escherichia coli* ribonucleotide reductase by time-resolved physical biochemical methods and X-ray crystallography, Biochemistry 37 (1998) 5840–5848.

[36] N. Mitic, M.D. Clay, L. Saleh, J.M. Bollinger Jr., E.I. Solomon, Spectroscopic and electronic structure studies of intermediate X in ribonucleotide reductase R2 and two variants: a description of the FeIV–oxo bond in the FeIII–O–FeIV dimer, J. Am. Chem. Soc. 129 (2007) 9049–9065.

[37] N. Voevodskaya, F. Lendzian, A. Ehrenberg, A. Gräslund, High catalytic activity achieved with a mixed manganese–iron site in protein R2 of chlamydia ribonu- cleotide reductase, FEBS Lett. 581 (2007) 3351–3355.

[38] M. Grabolle, M. Müller, C. Müller, P. Liebisch, H. Dau, Rapid loss of structural motifs in the manganese complex of oxygenic photosynthesis by X-ray irradia- tion at 10–300 K, J. Biol. Chem. 281 (2006) 4580–4588.

[39] S. Macedo, M. Pechlaner, W. Schmid, M. Weik, K. Sato, C. Dennison, K. Djinovic- Carugo, Can soaked-in scavengers protect metalloprotein active sites from re- duction during data collection? J. Synchrotron Radiat. 16 (2009) 191–204.

[40] M. Sommerhalter, R.L. Lieberman, A.C. Rosenzweig, X-ray crystallography and biological metal centers: is seeing believing? Inorg. Chem. 44 (2005) 770–778.

[41] H.H. Thorp, Bond valence sum analysis of metal–ligand bond lengths in metal- loenzymes and model complexes, Inorg. Chem. 31 (1992) 1585–1588.

[42] R.W. Strange, M.C. Feiters, Biological X-ray absorption spectroscopy (BioXAS): a valuable tool for the study of trace elements in the life sciences, Curr. Opin. Struct. Biol. 18 (2008) 609–616.

[43] H. Dau, M. Haumann, The manganese complex of photosystem ii in its reaction cycle—basic framework and possible realization at the atomic level, Coord. Chem. Rev. 252 (2008) 273–295.

[44] S. Bordiga, F. Bonino, K.P. Lillerud, C. Lamberti, X-ray absorption spectroscopies: useful tools to understand metallorganic frameworks structure and reactivity, Chem. Soc. Rev. 39 (2010) 4885–4927.

[45] J.M. Younker, C.M. Krest, W. Jiang, C. Krebs, J.M. Bollinger Jr., M.T. Green, Structural analysis of the Mn(IV)/Fe(III) cofactor of *Chlamydia trachomatis* ribonucleotide re- ductase by extended X-ray absorption fine structure spectroscopy and density functional theory calculations, J. Am. Chem. Soc. 130 (2008) 15022–15027.

[46] J. Baldwin, W.C. Voegtli, N. Khidekel, P. Moenne-Loccoz, C. Krebs, A.S. Pereira, B.A. Ley, B.H. Huynh, T.M. Loehr, P.J. Riggs-Gelasco, A.C. Rosenzweig, J.M. Bollin- ger Jr., Rational reprogramming of the R2 subunit of *Escherichia coli* ribonucleo- tide reductase into a self-hydroxylating monooxygenase, J. Am. Chem. Soc. 123 (2001) 7017–7030.

[47] T.L. Stemmler, T.M. Sossong Jr., J.I. Goldstein, D.E. Ash, T.E. Elgren, D.M. Kurtz Jr., J.E. Penner-Hahn, EXAFS comparison of the dimanganese core structures of manganese catalase, arginase, and manganese-substituted ribonucleotide re- ductase and hemerythrin, Biochemistry 36 (1997) 9847–9858.

[48] P.J. Riggs-Gelasco, L.J. Shu, S.X. Chen, D. Burdi, B.H. Huynh, L. Que, J. Stubbe, EXAFS characterization of the intermediate X generated during the assembly of the *Escherichia coli* ribonucleotide reductase R2 diferric tyrosyl radical cofac- tor, J. Am. Chem. Soc. 120 (1998) 849–860.

[49] J. Baldwin, C. Krebs, L. Saleh, M. Stelling, B.H. Huynh, J.M. Bollinger, P. Riggs- Gelasco, Structural characterization of the peroxodiiron(III) intermediate gener- ated during oxygen activation by the W48A/D84E variant of ribonucleotide re- ductase protein R2 from *Escherichia coli*, Biochemistry 42 (2003) 13269–13279.

[50] G.J. Mann, A. Gräslund, E.I. Ochiai, R. Ingemarson, L. Thelander, Purification and characterization of recombinant mouse and herpes-simplex virus ribonucleo- tide reductase R2 subunit, Biochemistry 30 (1991) 1939–1947.

[51] W. Jiang, J. Xie, H. Norgaard, J.M. Bollinger Jr., C. Krebs, Rapid and quantitative activation of *Chlamydia trachomatis* ribonucleotide reductase by hydrogen per- oxide, Biochemistry 47 (2008) 4477–4483.

[52] R. Klockenkämper, Total Reflection X-ray Fluorescence Analysis, Wiley-VCH, London, UK, 1996.

[53] S. Stoll, A. Schweiger, EasySpin, a comprehensive software package for spectral simulation and analysis in EPR, J. Magn. Reson. 178 (2006) 42–55.

[54] S. Todorovic, M.C. Justino, G. Wellenreuther, P. Hildebrandt, D.H. Murgida, W. Meyer-Klaucke, L.M. Saraiva, Iron–sulfur repair YTFE protein from *Escherichia coli*: structural characterization of the di-iron center, J. Biol. Inorg. Chem. 13 (2008) 765–770.

[55] S. Stripp, O. Sanganas, T. Happe, M. Haumann, The structure of the active site H- cluster of [FeFe] hydrogenase from the green alga *Chlamydomonas reinhardtii* studied by X-ray absorption spectroscopy, Biochemistry 48 (2009) 5042–5049.

[56] M. Haumann, C. Muller, P. Liebisch, L. Iuzzolino, J. Dittmer, M. Grabolle, T. Neisius, W. Meyer-Klaucke, H. Dau, Structural and oxidation state changes of the photo- system II manganese complex in four transitions of the water oxidation cycle (S0 –> S1, S1 –> S2, S2 –> S3, and S3,4 –> S0) characterized by X-ray absorp- tion spectroscopy at 20 K and room temperature, Biochemistry 44 (2005) 1894–1908.

[57] H. Dau, P. Liebisch, M. Haumann, X-ray absorption spectroscopy to analyze nu- clear geometry and electronic structure of biological metal centers—potential and questions examined with special focus on the tetra-nuclear manganese complex of oxygenic photosynthesis, Anal. Bioanal. Chem. 376 (2003) 562–583.

[58] S.I. Zabinsky, J.J. Rehr, A.L. Ankudinov, R.C. Albers, M.J. Eller, Multiple-scattering calculations of X-ray-absorption spectra, Phys. Rev. B 52 (1995) 2995–3009.

[59] J.J. Rehr, Theory and calculations of X-ray spectra: XAS, XES, XRS, and NRIXS, Radiat. Phys. Chem. 75 (2006) 1547–1558.

[60] K.V. Klementiev, XANES Dactyloscope for Windows, freeware, www.cells.es/ Beamlines/CLAESS/software/xanda.html2011.

[61] J.C. Swarbrick, Y. Kvashnin, K. Schulte, K. Seenivasan, C. Lamberti, P. Glatzel, Ligand identification in titanium complexes using X-ray valence-to-core emis- sion spectroscopy, Inorg. Chem. 49 (2010) 8323–8332.

[62] M. Haumann, P. Liebisch, C. Müller, M. Barra, M. Grabolle, H. Dau, Photosynthetic O$_2$ formation tracked by time-resolved X-ray experiments, Science 310 (2005) 1019–1021.

[63] E. Stavitski, F.M. de Groot, The CTM4XAS program for EELS and XAS spectral shape analysis of transition metal L-edges, Micron 41 (2010) 687–694.

[64] W.T. Liu, H.H. Thorp, Bond valence sum analysis of metal–ligand bond lengths in metalloenzymes and model complexes.2. Refined distances and other enzymes, Inorg. Chem. 32 (1993) 4102–4105.

[65] G.J. Palenik, Bond valence sums in coordination chemistry using oxidation state independent R-0 values. A simple method for calculating the oxidation state of manganese in complexes containing only Mn–O bonds, Inorg. Chem. 36 (1997) 4888–4890.

[66] R.M. Wood, G.J. Palenik, Bond valence sums in coordination chemistry. A simple method for calculating the oxidation state of cobalt in complexes containing only Co–O bonds, Inorg. Chem. 37 (1998) 4149–4151.

[67] S. Lauchan, T.J. Prior, S. Meansiri, A. Rujiwatra, Cobalt(ethylenediamine)sulfate: a pillared layered coordination polymer, J. Inorg. Organomet. Polym. Mater. 18 (2008) 352–357.

[68] J.E. Readman, I. Gaineson, J.A. Hrijac, P.A. Anderson, Cationic zinc-cadmium alloy clusters in zeolite A, Microporous Mesoporous Mater. 104 (2007) 83–88.

[69] F. Neese, Orca: an ab-initio, DFT, and semiempirical electronic structure package. V.2.6.35, Theoretical Chemistry Group, University of Bonn, Bonn, Germany, 2008.

[70] P. Chernev, I. Zaharieva, H. Dau, M. Haumann, Carboxylate shifts steer interquinone electron transfer in photosynthesis, J. Biol. Chem. 286 (2011) 5368–5374.

[71] A.D. Becke, Density-functional exchange-energy approximation with correct asymptotic behavior, Phys. Rev. A 38 (1988) 3098.

[72] A. Schäfer, C. Huber, R. Ahlrichs, Fully optimized contracted Gaussian basis sets of triple zeta valence quality for atoms Li to Kr, J. Chem. Phys. 100 (1994) 5829–5835.

[73] F. Weigend, Accurate Coulomb-fitting basis sets for H to Rn, Phys. Chem. Chem. Phys. 8 (2006) 1057–1065.

[74] S. Sinnecker, A. Rajendran, A. Klamt, M. Diedenhofen, F. Neese, Calculation of solvent shifts on electronic g-tensors with the conductor-like screening model (COSMO) and its self-consistent generalization to real solvents (direct COSMO-RS), J. Phys. Chem. A 110 (2006) 2235–2245.

[75] P. Seal, S. Chakrabarti, Magnetic interactions in alkyl substituted cyclohexane diradical systems: a broken symmetry approach, J. Phys. Chem. A 112 (2008) 3409–3413.

[76] S. Sinnecker, F. Neese, L. Noodleman, W. Lubitz, Calculating the electron paramagnetic resonance parameters of exchange coupled transition metal complexes using broken symmetry density functional theory: application to a MnIII/MnIV model compound, J. Am. Chem. Soc. 126 (2004) 2613–2622.

[77] A. Popovic-Bijelic, N. Voevodskaya, V. Domkin, L. Thelander, A. Gräslund, Metal binding and activity of ribonucleotide reductase protein R2 mutants: conditions for formation of the mixed manganese-iron cofactor, Biochemistry 48 (2009) 6532–6539.

[78] Y.H. Dong, H. Fujii, M.P. Hendrich, R.A. Leising, G.F. Pan, C.R. Randall, E.C. Wilkinson, Y. Zang, L. Que, B.G. Fox, K. Kauffmann, E. Munck, A high-valent nonheme iron intermediate—structure and properties of [Fe2(μ-O)2(5-Me-TPA)2](ClO4)3, J. Am. Chem. Soc. 117 (1995) 2778–2792.

[79] R.A. Leising, B.A. Brennan, L. Que, E. Munck, Models for nonheme iron oxygenases—a high-valent iron oxo intermediate, J. Am. Chem. Soc. 113 (1991) 3988–3990.

[80] L. Que, W.B. Tolman, Bis(μ-O)dimetal "Diamond" cores in copper and iron complexes relevant to biocatalysis, Angew. Chem. Int. Ed Engl. 41 (2002) 1114–1137.

[81] J. Sanders-Loehr, W.D. Wheeler, A.K. Shiemke, B.A. Averill, T.M. Loehr, Electronic and Raman-spectroscopic properties of oxo-bridged dinuclear iron centers in proteins and model compounds, J. Am. Chem. Soc. 111 (1989) 8084–8093.

[82] D.M. Kurtz, Oxo-bridged and hydroxo-bridged diiron complexes—a chemical perspective on a biological unit, Chem. Rev. 90 (1990) 585–606.

[83] B.M. Sjöberg, J. Sanders-Loehr, T.M. Loehr, Identification of a hydroxide ligand at the iron center of ribonucleotide reductase by resonance Raman spectroscopy, Biochemistry 26 (1987) 4242–4247.

[84] J.A. Broadwater, J. Ai, T.M. Loehr, J. Sanders-Loehr, B.G. Fox, Peroxodiferric intermediate of stearoyl-acyl carrier protein delta 9 desaturase: oxidase reactivity during single turnover and implications for the mechanism of desaturation, Biochemistry 37 (1998) 14664–14671.

[85] P. Moenne-Loccoz, C. Krebs, K. Herlihy, D.E. Edmondson, E.C. Theil, B.H. Huynh, T.M. Loehr, The ferroxidase reaction of ferritin reveals a diferric mu-1,2 bridging peroxide intermediate in common with other O-2-activating non-heme diiron proteins, Biochemistry 38 (1999) 5290–5295.

[86] A.J. Skulan, T.C. Brunold, J. Baldwin, L. Saleh, J.M. Bollinger, E.I. Solomon, Nature of the peroxo intermediate of the W48F/D84E ribonucleotide reductase variant: implications for O2 activation by binuclear non-heme iron enzymes, J. Am. Chem. Soc. 126 (2004) 8842–8855.

[87] J. Terner, V. Palaniappan, A. Gold, R. Weiss, M.M. Fitzgerald, A.M. Sullivan, C.M. Hosten, Resonance Raman spectroscopy of oxoiron(IV) porphyrin Pi-cation radical and oxoiron(IV) hemes in peroxidase intermediates, J. Inorg. Biochem. 100 (2006) 480–501.

[88] W. Jiang, J.J. Xie, P.T. Varano, C. Krebs, J.M. Bollinger, Two distinct mechanisms of inactivation of the class Ic ribonucleotide reductase from Chlamydia trachomatis by hydroxyurea: implications for the protein gating of intersubunit electron transfer, Biochemistry 49 (2010) 5340–5349.

[89] S. Khangulov, M. Sivaraja, V.V. Barynin, G.C. Dismukes, The dimanganese(III, IV) oxidation-state of catalase from Thermus thermophilus—electron nuclear double-resonance analysis of water and protein ligands in the active-site, Biochemistry 32 (1993) 4912–4924.

[90] C. Teutloff, K.O. Schafer, S. Sinnecker, V. Barynin, R. Bittl, K. Wieghardt, F. Lendzian, W. Lubitz, High-field EPR investigations of (MnMnIV–MnII and MnIVMnII and MnIIIMnII states of dimanganese catalase and related model systems, Magn. Reson. Chem. 43 (2005) S51–S64.

[91] N. Voevodskaya, F. Lendzian, A. Gräslund, A stable FeIII–FeIV replacement of tyrosyl radical in a class I ribonucleotide reductase, Biochem. Biophys. Res. Commun. 330 (2005) 1213–1216.

[92] B.J.S. Gaffney, H. J., Simulation of the EMR spectra of high-spin iron in proteins, in: L.J.R. Berliner, J. (Eds.), EMR of Paramagnetic Molecules, Plenum Press, New York, 1993, pp. 1–57.

[93] J.J. Danford, P. Dobrowolski, L.M. Berreau, Thioester hydrolysis reactivity of an Fe(III)Zn(II) complex, Inorg. Chem. 48 (2009) 11352–11361.

[94] P. Liebisch, H. Dau, Linear dichroism in the XANES of partially oriented samples: theory and application to the photosynthetic manganese complex, Chemphyschem 11 (2010) 1236–1247.

[95] T.E. Westre, P. Kennepohl, J.G. DeWitt, B. Hedman, K.O. Hodgson, E.I. Solomon, A multiplet analysis of Fe K-edge 1s->3d pre-edge features of iron complexes, J. Am. Chem. Soc. 119 (1997) 6297–6314.

[96] P. Afanasiev, E.V. Kudrik, J.M.M. Millet, D. Bouchu, A.B. Sorokin, High-valent diiron species generated from n-bridged diiron phthalocyanine and H2O2, Dalton Trans. 40 (2011) 701–710.

[97] K.D. Koehntop, J.U. Rohde, M. Costas, L. Que, XAS characterization of end-on and side-on peroxoiron(III) complexes of the neutral pentadentate n-donor ligand n-methyl-n,n′,n′-tris(2-pyridylmethyl)ethane-1,2-diamine, Dalton Trans. (2004) 3191–3198.

[98] E.I. Solomon, X.J. Xie, A. Dey, Mixed valent sites in biological electron transfer, Chem. Soc. Rev. 37 (2008) 623–638.

[99] K.K. Gunter, L.M. Miller, M. Aschner, R. Eliseev, D. Depuis, C.E. Gavin, T.E. Gunter, XANES spectroscopy: a promising tool for toxicology: a tutorial, Neurotoxicology 23 (2002) 127–146.

[100] N. Lee, T. Petrenko, U. Bergmann, F. Neese, S. DeBeer, Probing valence orbital composition with iron K beta X-ray emission spectroscopy, J. Am. Chem. Soc. 132 (2010) 9715–9727.

[101] P. Glatzel, U. Bergmann, High resolution 1s core hole X-ray spectroscopy in 3d transition metal complexes—electronic and structural information, Coord. Chem. Rev. 249 (2005) 65–95.

[102] P. Glatzel, L. Jacquamet, U. Bergmann, F.M.F. de Groot, S.P. Cramer, Site-selective EXAFS in mixed-valence compounds using high-resolution fluorescence detection: a study of iron in Prussian blue, Inorg. Chem. 41 (2002) 3121–3127.

[103] G.D. Pirngruber, J.D. Grunwaldt, J.A. van Bokhoven, A. Kalytta, A. Reller, O.V. Safonova, P. Glatzel, On the presence of Fe(IV) in Fe-ZSM-5 and FeSrO3−x—unequivocal detection of the 3d4 spin system by resonant inelastic X-ray scattering, J. Phys. Chem. B 110 (2006) 18104–18107.

[104] S.D. Gamblin, D.S. Urch, Metal K beta X-ray emission spectra of first row transition metal compounds, J. Electron Spectr. Relat. Phenom. 113 (2001) 179–192.

[105] I. Zaharieva, P. Chernev, M. Risch, G. Gerencser, G. Berggren, G. Shevchenko, M. Anderlund, T.-C. Weng, M. Haumann, H. Dau, Towards a comprehensive X-ray approach for studying the photosynthetic manganese complex—XANES, K-alpha/K-beta/K-beta-satellite emission lines, RIXS, and comparative computational approaches for selected model complexes, J. Phys. Conf. Ser. 190 (2009) 012142.

[106] S.J. George, J.X. Fu, Y.S. Guo, O.B. Drury, S. Friedrich, T. Rauchfuss, P.I. Volkers, J.C. Peters, V. Scott, S.D. Brown, C.M. Thomas, S.P. Cramer, X-ray photochemistry in iron complexes from Fe(0) to Fe(IV)—can a bug become a feature? Inorg. Chim. Acta 361 (2008) 1157–1165.

[107] M. Grabolle, H. Dau, Energetics of primary and secondary electron transfer in photosystem II membrane particles of spinach revisited on basis of recombination-fluorescence measurements, Biochim. Biophys. Acta 1708 (2005) 209–218.

[108] I. Vass, S. Styring, pH-dependent charge equilibria between tyrosine-D and the S states in photosystem II. Estimation of relative midpoint redox potentials, Biochemistry 30 (1991) 830–839.

[109] W.G. Han, D.A. Giammona, D. Bashford, L. Noodleman, Density functional theory analysis of structure, energetics, and spectroscopy for the Mn–Fe active site of Chlamydia trachomatis ribonucleotide reductase in four oxidation states, Inorg. Chem. 49 (2010) 7266–7281.

[110] W.G. Han, L. Noodleman, DFT calculations of comparative energetics and ENDOR/Mössbauer properties for two protonation states of the iron dimer cluster of ribonucleotide reductase intermediate X, Dalton Trans. (2009) 6045–6057.

[111] H.F. Hsu, Y.H. Dong, L.J. Shu, V.G. Young, L. Que, Crystal structure of a synthetic high-valent complex with an Fe2(μ-O)2 diamond core. Implications for the core structures of methane monooxygenase intermediate Q and ribonucleotide reductase intermediate X, J. Am. Chem. Soc. 121 (1999) 5230–5237.

[112] M. Merkx, D.A. Kopp, M.H. Sazinsky, J.L. Blazyk, J. Muller, S.J. Lippard, Dioxygen activation and methane hydroxylation by soluble methane monooxygenase: a tale of two irons and three proteins, Angew. Chem. Int. Ed Engl. 40 (2001) 2782–2807.

[113] L.J. Shu, J.C. Nesheim, K. Kauffmann, E. Munck, J.D. Lipscomb, L. Que, An Fe2IVO2 diamond core structure for the key intermediate Q of methane monooxygenase, Science 275 (1997) 515–518.

[114] M. Shanmugam, P.E. Doan, N.S. Lees, J. Stubbe, B.M. Hoffman, Identification of protonated oxygenic ligands of ribonucleotide reductase intermediate X, J. Am. Chem. Soc. 131 (2009) 3370–3376.

[115] D. Yun, R. Garcia-Serres, B.M. Chicalese, Y.H. An, B.H. Huynh, J.M. Bollinger, (mu-1,2-peroxo)diiron(III/III) complex as a precursor to the diiron(III/IV) intermediate X in the assembly of the iron-radical cofactor of ribonucleotide reductase from mouse, Biochemistry 46 (2007) 1925–1932.

[116] W.G. Han, T. Liu, T. Lovell, L. Noodleman, Active site structure of class I ribonucleotide reductase intermediate X: a density functional theory analysis of structure, energetics, and spectroscopy, J. Am. Chem. Soc. 127 (2005) 15778–15790.

[117] D. Burdi, J.-P. Willems, P. Riggs-Gelasco, W.E. Antholine, J. Stubbe, B.M. Hoffman, The core structure of X generated in the assembly of the diiron cluster of ribonucleotide reductase: 17O2 and H2 17O ENDOR, J. Am. Chem. Soc. 120 (1998) 12910–12919.

[118] W. Jiang, J.M. Bollinger Jr., C. Krebs, The active form of *Chlamydia trachomatis* ribonucleotide reductase R2 protein contains a heterodinuclear Mn(IV)/Fe(III) cluster with S = 1 ground state, J. Am. Chem. Soc. 129 (2007) 7504–7505.

[119] K. Roos, P.E. Siegbahn, Oxygen cleavage with manganese and iron in ribonucleotide reductase from *Chlamydia trachomatis*, J. Biol. Inorg. Chem. 16 (2011) 553–565.

[120] M. Högbom, M.E. Andersson, P. Nordlund, Crystal structures of oxidized dinuclear manganese centres in Mn-substituted class I ribonucleotide reductase from *Escherichia coli*: carboxylate shifts with implications for O-2 activation and radical generation, J. Biol. Inorg. Chem. 6 (2001) 315–323.

[121] W.C. Voegtli, M. Sommerhalter, L. Saleh, J. Baldwin, J.M. Bollinger Jr., A.C. Rosenzweig, Variable coordination geometries at the diiron(II) active site of ribonucleotide reductase R2, J. Am. Chem. Soc. 125 (2003) 15822–15830.

[122] N. Cox, H. Ogata, P. Stolle, E. Reijerse, G. Auling, W. Lubitz, A tyrosyl-dimanganese coupled spin system is the native metalloradical cofactor of the R2f subunit of the ribonucleotide reductase of *Corynebacterium ammoniagenes*, J. Am. Chem. Soc. 132 (2010) 11197–11213.

[123] A.K. Boal, J.A. Cotruvo, J. Stubbe, A.C. Rosenzweig, Structural basis for activation of class Ib ribonucleotide reductase, Science 329 (2010) 1526–1530.

[124] X.D. Wang, L. Que, Extended X-ray absorption fine structure studies of the anion complexes of FeZn uteroferrin, Biochemistry 37 (1998) 7813–7821.

[125] J. Yano, J. Kern, K.-D. Irrgang, M.J. Latimer, U. Bergmann, P. Glatzel, Y. Pushkar, J. Biesiadka, B. Loll, K. Sauer, J. Messinger, A. Zouni, V.K. Yachandra, X-ray damage to the Mn_4Ca complex in single crystals of photosystem II: a case study for metalloprotein crystallography, Proc. Natl. Acad. Sci. U. S. A. 102 (2005) 12047–12052.

[126] W. Jiang, D. Yun, L. Saleh, J.M. Bollinger Jr., C. Krebs, Formation and function of the manganese(IV)/iron(III) cofactor in *Chlamydia trachomatis* ribonucleotide reductase, Biochemistry 47 (2008) 13736–13744.

[127] J. Messinger, J.H. Robblee, U. Bergmann, C. Fernandez, P. Glatzel, H. Visser, R.M. Cinco, K.L. McFarlane, E. Bellacchio, S.A. Pizarro, S.P. Cramer, K. Sauer, M.P. Klein, V.K. Yachandra, Absence of Mn-centered oxidation in the S2 -> S3 transition: implications for the mechanism of photosynthetic water oxidation, J. Am. Chem. Soc. 123 (2001) 7804–7820.

[128] P. Huang, J. Högblom, M.F. Anderlund, L. Sun, A. Magnuson, S. Styring, Light-induced multistep oxidation of dinuclear manganese complexes for artificial photosynthesis, J. Inorg. Biochem. 98 (2004) 733–745.

[129] A. Magnuson, P. Liebisch, J. Högblom, M.F. Anderlund, R. Lomoth, W. Meyer-Klaucke, M. Haumann, H. Dau, Bridging-type changes facilitate successive oxidation steps at about 1 V in two binuclear manganese complexes—implications for photosynthetic water oxidation, J. Inorg. Biochem. 100 (2006) 1234–1243.